Science Advances
AAAS

Supplementary Materials for

Functional regulation of an intrinsically disordered protein via a conformationally excited state

Kulkarni Madhurima *et al.*

Corresponding author: Ashok Sekhar, ashoksekhar@iisc.ac.in

Sci. Adv. **9**, eadh4591 (2023)
DOI: 10.1126/sciadv.adh4591

This PDF file includes:

Supplementary Text

Extracting ^{1}H-^{15}N RDCs using $^{1}H^{N}$ CEST experiments

While ^{15}N CEST experiments have been used to determine excited state ^{1}H-^{15}N RDCs in the context of nucleic acids (*49*), $^{1}H^{N}$ CEST has not been explored so far as a way to extract RDCs in the excited state. In the method of obtaining $^{1}H^{N}$ CEST profiles reported here (Fig. S13, (*91*), a weak RF field is applied on initial H_z magnetization, while $2H_zN_z$ is detected at the end of the exchange duration (T_{ex}). ^{15}N decoupling is not employed during the exchange period, so that a peak and a trough, (analogous to the spectrum of antiphase magnetization) are obtained for the ground and excited states that are separated by $^{1}J_{NH}$ in each state respectively. The four extrema are then fit to sums of Lorentzians to extract offset positions for each extremum from which $^{1}J_{NH}$ values in both the ground and excited states are calculated. These experiments are repeated for unaligned and aligned samples and the difference in $^{1}J_{NH}$ gives the RDC (Fig. S13).

In order to evaluate the robustness of this method, we simulated $^{1}H^{N}$ CEST profiles using exchange parameters observed for $CytR^{N}$ and experimental parameters employed for extracting ^{1}H-^{15}N RDCs. $k_{ex,DE}$ and p_E were set to 50 s^{-1} and 10 % respectively. Input $^{1}H^{N}$ $\Delta\varpi_{DE}$ values in the simulation ranged from 0.311 to 1.215 ppm, since RDCs were calculated only for those residues where $^{1}H^{N}$ $\Delta\varpi_{DE}$ > 0.3 ppm and the largest $\Delta\varpi_{DE}$ for $CytR^{N}$ observed experimentally was 1.215 ppm. Each $\Delta\varpi_{DE}$ was input along with the respective $^{1}J_{NH}$ in unaligned, PAG and C_8E_5/octanol samples. For example, the $\Delta\varpi_{GE}$, $^{1}J_{NH}$(unaligned), $^{1}J_{NH}$(PAG) and $^{1}J_{NH}$(C_8E_5/octanol) for T11 were input as 1.215 ppm, 91.7 Hz, 92.8 Hz and 98 Hz as seen in experiment. Noise was added into the simulated data based on the average S/N of each experiment, with the minimum S/N being 292 for the sample aligned in C_8E_5/octanol. All simulations were carried out at a ^{1}H Larmor frequency of 700 MHz, 15 Hz B_1 field strength and 500 ms exchange time. B_1 inhomogeneity was modeled as described previously (*40*). The simulated $^{1}H^{N}$ CEST profiles were then fit to sums of four Lorentzians to extract $^{1}J_{NH}$ and RDCs for each residue were calculated as the differences between the unaligned and aligned $^{1}J_{NH}$. The correlation between the input RDCs and the values obtained from the fitting procedure is excellent (Fig. S14A) with overall RMSDs of 0.3 and 0.7 Hz for PAG and C_8E_5/octanol, respectively. These simulations confirm that modeling CEST dips as Lorentzians

is a reliable way of extracting $^1J_{NH}$ from $^1H^N$ CEST profiles under our conditions of $k_{ex,DE}$, p_E, $\Delta\varpi_{GE}$, B_1 and S/N values.

We next addressed the question of how large $^1H^N$ $\Delta\varpi_{GE}$ should be in order to quantitatively extract $^1J_{NH}$ from $^1H^N$ CEST profiles. We simulated $^1H^N$ CEST profiles with $\Delta\varpi_{GE}$ varying from 0.15 – 0.6 ppm on a 700 MHz spectrometer using a 15 Hz CEST B_1 field. Two different values of $^1J_{NH,ES}$, 66 and 96 Hz, were used in the simulations as representatives of the largest and smallest Δ^1J_{NH} ($= {}^1J_{NH,ES} - {}^1J_{NH,GS}$) seen in experiments, while $^1J_{NH,GS}$ was kept constant at 93 Hz. Noise corresponding to the lowest S/N observed experimentally (S/N = 292) was added to the simulated data. Simulated $^1H^N$ CEST profiles were then fit to sums of four Lorentzians as described above and fit $^1J_{NH,ES}$ values were compared to the input (Fig. S14B). The fit values match the input well to within 1.5 Hz for $\Delta\varpi_{DE} \geq 0.3$ ppm. Systematic differences emerge at $\Delta\varpi_{DE} = 0.2$ ppm and fit values are dramatically incorrect for $\Delta\varpi_{DE} = 0.15$ ppm and lower. These trends are not dependent on the magnitude of Δ^1J_{NH} for $^1J_{NH,GS} = 93$ Hz. In practice, we have analyzed $^1H^N$ CEST profiles only from residues for which $^1H^N$ $\Delta\varpi_{DE} > 0.3$ ppm, where the maximum deviation in $^1J_{NH}$ from the correct value is expected to be ~ 1.5 Hz.

The reason for the large systematic errors in $^1J_{NH}$ at small $\Delta\varpi_{DE}$ becomes evident when looking at the $^1H^N$ CEST profiles as a function of $\Delta\varpi_{DE}$ (Fig. S14C). For large $\Delta\varpi_{DE} > 0.3$ ppm, the four CEST dips are sufficiently separated from each other for the dip positions to be extracted reliably by modeling them as Lorentzians. For $\Delta\varpi_{DE}$ ~ 0.15 ppm (corresponding to 105 Hz on a 700 MHz spectrometer), the positive dip of the ground state overlaps with the negative dip of the excited state because $\Delta\varpi_{DE} = 0.15ppm = 105Hz \cong {}^1J_{NH}$. This results in partial cancellation of the dips and an inability to correctly localise the frequencies of all four extrema simultaneously.

Structure calculations using CS-Rosetta

The structure of the excited state of $CytR^N$ was calculated using a standard CS-Rosetta structure calculation protocol within the CS-Rosetta Toolbox 3.0 (*53*).

Selecting the $CytR^N$ segment for structure calculation. Order parameters derived from excited state chemical shifts (Fig. 2G) indicate that S^2 values are smaller than 0.5 at the N-terminus (M1-M12) and C-terminus (P57-E66). The trends in order parameters agree with chemical shift

perturbations (Fig. 2F), which indicate that residues before T11 and beyond Q56 do not change in chemical shift when the native state transitions to the excited conformation. Accordingly, we calculated structures for two segments of $CytR^N$, 11-53 and 11-57. Since the structures of the two segments are virtually identical (Fig. S16A) and the region between 54-57 does not participate in secondary structure or tertiary interactions, all subsequent descriptions below pertain to the structure calculation protocol for $CytR^N$(11-53).

Fragment picking. As the first step, a fragment library containing 200 3-amino acid fragments and 200 9-residue fragments was constructed for each residue position of $CytR^N$(11-53) using the pick_fragments module(*53*). 34 ^{15}N, 33 $^{1}H^N$, 25 $^{13}C\alpha$ and 27 $^{13}C'$ chemical shifts were used as inputs at this stage. Fragments are chosen from a database containing segments of X-ray structures using the similarity of the secondary structure predicted by TALOS-N (*92*) for the target sequence with the X-ray structure as the primary guide. The selected fragments are subsequently scored based on how well their sequence, secondary structure and chemical shifts (predicted by Sparta+) (*54*) match with the target. Homologous structures were eliminated from the database during fragment picking using the -nohom flag in order to avoid biasing the structure calculation.

Fragment assembly. The fragment library was then used along with 119 chemical shifts and 65 RDCs as inputs for the fragment assembly with the 'abrelax' tool (*53*). Structure calculation with Abrelax consists of two stages: in the first stage (Abinitio), a coarse-grained conformational search is performed to obtain low-resolution structural models that are scored using a 'centroid' scoring function; in the next stage (Relax), the structure undergoes all-atom refinement in the Rosetta force field. The CS-Rosetta scoring function was modified to incorporate an energy term arising from deviations of predicted RDCs from experimental values. The weighting factor for this deviation was adjusted so that the width of the resulting distributions of energy contributions from chemical shifts and RDCs are approximately equal (*93*). The RDC weighting factor was the same for both the Abinitio and the Relax stages of structure calculation.

Analysis of structures. 10000 structures of $CytR^N$(11-53) were calculated using the above protocol. The structures were then rescored according to the deviations of their Sparta+-predicted chemical shifts from the experimental values using Eq. 1 of Shen *et al.* (*52*). The energy vs RMSD (to the lowest energy structure) shows a well-defined convergence funnel

(Figure S16B) The 10 structures (*93*) with the lowest scores were used as descriptors of the excited state ensemble. The quality of the structures was checked with the PSVS Validation Suite (*94*).

In order to determine how well the excited state structure agrees with input experimental data, we first back-predicted the ^{15}N, $^{1}H^{N}$, $^{13}C\alpha$ and $^{13}C'$ chemical shifts for the lowest energy conformer from CS-Rosetta using Sparta+. The shifts agree well with the experimental values (Fig. S17) and the RMSDs for all nuclei (^{15}N: 1.95 ppm, $^{1}H^{N}$: 0.38 ppm, $^{13}C'$: 1.09 ppm, $^{13}C\alpha$: 0.58 ppm) are within the performance of the Sparta+ neural network (*54*) (^{15}N: 2.45 ppm, $^{1}H^{N}$: 0.49 ppm, $^{13}C'$: 1.09 ppm, $^{13}C\alpha$: 0.94 ppm).

We next used PALES (*55*) to predict the RDCs for the excited state by fitting the measured RDCs to the final excited state structure and using the optimized alignment tensor to evaluate the RDCs. The predicted RDCs agree very well with the experimental RDCs (Figs. 3D, S18), with an RMSD of 0.87 Hz for PAG and 1.26 Hz for C_8E_5/octanol. The Cornilescu quality factor (Q) values (*95*) for the fits are 0.124 and 0.091 for PAG and C_8E_5/octanol respectively, demonstrating that there is good agreement between the experimental RDCs and the RDCs calculated from the excited state structure.

In order to assess the differences in alignment of $CytR^{N}$ in PAG and C_8E_5/octanol, we calculated the scalar product between the respective alignment tensors (*96*). A modest value of 0.83 was obtained, indicating that there is a pronounced correlation in the information content between the RDCs collected in the two media. Nevertheless, the RDCs in the two media were obtained using distinct sample preparation strategies (stretched gels versus liquid crystals) and they are not entirely collinear. Considering that NMR-derived restraints for the excited state structure calculation are sparse (119 backbone chemical shifts and 65 RDCs for a 50 amino acid sequence) because of the inability to collect NOEs in the excited state, we have incorporated both sets of RDCs in the CS-Rosetta structure calculation protocol to improve reliability and confidence in the structure.

Flux calculations. The flux of molecules reaching the specific DNA-$CytR^{N}$ complex through the D→B and E→B pathways was calculated from the rate constants ($k_{ex,DB}$, $k_{ex,EB}$) and populations (p_E, p_B) obtained by fitting CEST and DRD-CEST data as described in Materials

and Methods, along with the total protein (P_T) and DNA concentration (D_T) in Sample 5. The rate constant $k_{ex,EB}$ is related to the association rate constant between the excited state and DNA, $k_{on,EB}$ as:

$$k_{on,EB} = \frac{k_{EB}}{[DNA]} = \left(\frac{k_{ex,EB}}{[DNA]}\right)\left(\frac{p_B}{p_B + p_E}\right)$$

Here,

$$k_{ex,EB} = k_{EB} + k_{BE} = k_{on,EB}[DNA] + k_{BE}$$

Similarly,

$$k_{on,DB} = \frac{k_{DB}}{[DNA]} = \left(\frac{k_{ex,DB}}{[DNA]}\right)\left(\frac{p_B}{p_B + p_D}\right)$$

Here, $[i]$ is the equilibrium concentration of species *i*. From the mass balance equations,

$$[DNA] = D_T - [B] = D_T - P_T p_B$$

The flux along the E→B and D→B pathways are given by:

$$\phi_{EB} = k_{on,EB}[E][DNA]$$

and

$$\phi_{DB} = k_{on,DB}[D][DNA]$$

The ratio of the flux along the D→B and E→B pathways (Φ) is then given by:

$$\Phi = \frac{\phi_{EB}}{\phi_{DB}} = \frac{k_{on,EB}[E][DNA]}{k_{on,DB}[D][DNA]} = \left(\frac{k_{ex,EB}}{k_{ex,DB}}\right)\left(\frac{p_E}{p_D}\right)\left(\frac{p_D + p_B}{p_E + p_B}\right)$$

We calculated the flux ratio F in four different ways.

1. We first calculated Φ for the rate constant values obtained directly from the fit. Using the values $k_{ex,DB}$ = 0.00015 s^{-1}, $k_{ex,EB}$ = 194 s^{-1}, p_E = 0.16, p_B = 0.02 and $p_D = 1 - (p_E + p_B) = 0.82$, the ratio of flux along the E→B to the D→B pathways comes out to be 1.2 x 10^6.
2. Since p_E is slightly different from the value obtained in the absence of DNA because it was allowed to vary during the triangular fitting routine, we next calculated Φ using the p_E value determined from ^{15}N CEST experiments on DNA-free wt CytR (Sample 1, p_E = 0.087). p_E is a fractional ratio such that the sum of the populations of all conformations in the system is 1. Therefore, from the data on Sample 1,

$$\frac{p_E}{p_D} = \frac{0.087}{1 - 0.087} = 0.095$$

Using this ratio for the data on Sample 5, where three conformations D, E and B coexist in equilibrium, we get p_E = 0.085, p_B = 0.02 and $p_D = 1 - (p_E + p_B) = 0.89$. The flux ratio Φ from these populations, as well as the rate constants from above ($k_{ex,DB}$ =

0.00015 s^{-1}, $k_{ex,EB}$ = 194 s^{-1}), is evaluated to be 1.1 x 10^6, which is very similar to the value calculated in method 1 above.

The error in $k_{ex,DB}$ (0.3 s^{-1}) is much larger than the value itself (0.00015 s^{-1}), since the data-driven measure of $k_{ex,DB}$ is very close to 0. In the next two methods, we used a 3σ value as an estimate of the upper bound of $k_{ex,DB}$, where σ (=0.3 s^{-1}) is the error in $k_{ex,DB}$.

3. Using $k_{ex,DB}$=3σ=0.9 s^{-1} and the other parameters from method 1 ($k_{ex,EB}$ = 194 s^{-1}, p_E = 0.16, p_B = 0.02 and $p_D = 1 - (p_E + p_B) = 0.82$), the ratio of flux along the E→B to the D→B pathways is calculated to be 2.0 x 10^2.
4. Using $k_{ex,DB}$=3σ=0.9 s^{-1} and the other parameters from method 2 ($k_{ex,EB}$ = 194 s^{-1}, p_E = 0.085, p_B = 0.02 and $p_D = 1 - (p_E + p_B) = 0.89$), the ratio of flux along the E→B to the D→B pathways is evaluated to be 1.8 x 10^2.

Therefore, the limits on Φ imposed by the D- and DRD-CEST data on D34 in conjunction with the triangular model are between 1.8 x 10^2 and 1.2 x 10^6.

The conformational selection pathway is sometimes defined using the disordered state as the origin, rather than the state with the complementary conformation (the excited state E here) (*62*). In this case, the flux along the CS pathway (F_{CS}) is a combination of the flux along two serial reaction pathways D→E (ϕ_{DE}) and E→B (ϕ_{EB}) and is given by the equation (*62*):

$$\phi_{CS} = \left(\frac{1}{\phi_{DE}} + \frac{1}{\phi_{EB}}\right)^{-1},$$

where

$$\phi_{DE} = k_{DE}[D].$$

Using these equations, the flux ratio along the CS and IF pathways $\Phi = \frac{\phi_{CS}}{\phi_{IF}} = \frac{\phi_{CS}}{\phi_{DB}}$ comes out to be 7.8 x 10^5, 5.5 x 10^5, 1.3 x 10^2 and 0.9 x 10^2 for cases 1-4 above respectively.

CS and IF mechanisms are known to be dependent on the concentration of the ligand, with the CS mechanism dominating at lower ligand concentrations and a switch to the IF mechanism occurring at higher ligand concentrations (*62*). In order to determine the concentration dependence of the operative mechanism, we calculated the ratio $R = \frac{\phi_{CS}}{\phi_{CS}+\phi_{IF}} = \frac{\Phi}{1+\Phi}$ for total protein concentrations (P_T) between 1 pM and 1 mM, as well as for total DNA concentrations (D_T) between 1 nM and 1 M. R vs D_T curves are virtually identical in this range of P_T values and the switch between CS and IF mechanisms (R=0.5) occurs at a D_T value of ~ 50 mM (Fig.

S29). The typical DNA concentration in an *E.coli* cell is ~ 1 nM (*97, 98*) and the switch between mechanisms occurs at concentrations 6-7 orders of magnitude higher than this. Therefore, for all relevant DNA concentrations, conformational selection remains the operative mechanism for the CytR^N-DNA interaction.

Fitting RDC and chemical shift data to ensembles of structures. In order to derive more confidence in our CS-Rosetta model of the excited state, we fit the chemical shift (CS) and residual dipolar coupling (RDC) data to an ensemble of structures allowing the α-helices to fluctuate. As the first step in this procedure, we constructed a χ^2 function for determining goodness-of-fit based on deviations of the predicted values from experimental measurements in order to obtain a measure of fit quality across large ensembles. The χ^2 function is defined as:

$$\chi^2 = \chi^2_{RDC} + \chi^2_{CS}$$

where

$$\chi^2_{RDC} = \sum_{i=1}^{N_{RDC}} \left(\frac{RDC_{i,expt} - RDC_{i,pred}}{\sigma_{RDC}} \right)^2$$

and

$$\chi^2_{CS} = \sum_{i=1}^{N_{CS}} \left(\frac{CS_{i,expt} - CS_{i,pred}}{\sigma_{i,CS}} \right)^2$$

As the goodness-of-fit increases, the χ^2 function decreases and the agreement between the data and the model is better. Sparta+ (*54*) was used to predict chemical shifts from the structure and the nucleus-specific error in the prediction was used as $\sigma_{i,CS}$. PALES (*55*) was used to fit the alignment tensor to the structure and the best-fit tensor was used to predict residual dipolar couplings. The error in the RDC measurements (σ_{RDC}) was taken to be 1 Hz. The value of this χ^2 function for the CS-Rosetta excited state structure is 144.

Next, we fit a disordered 10-member CytR^N ensemble to the excited state RDC and chemical shifts to see if a structure lacking the three α-helices can accommodate the experimental data. χ^2 increases to values between 6300-7600, confirming that an ensemble comprising only disordered conformations does not agree well with the input CS and RDC data.

We then fit the CS and RDCs to the 10 lowest energy structures generated by CS-Rosetta during our structure calculation protocol (Fig. S16C). As expected from the close structural similarity between members of this CS-Rosetta ensemble, the χ^2 function varies only between 143 and 159 for these 10 structures.

In order to generate fluctuations of large magnitude in the α-helices, we next ran Monte Carlo simulations using the ABSINTH force field (*99*) for three million steps, saving 6001 frames overall. Simulations were done at 288 K at an ionic strength of 43 mM and a dielectric strength of 82. The χ^2 function was then calculated for the 6001 structures to determine the goodness-of-fit. Figure S19A shows an overlay of the 10 structures that agree best with the input chemical shifts and RDCs. These 10 best fit structures have all-atom RMSDs varying between 0.35 and 0.8 Å to the starting structure (the CS-Rosetta model), confirming that the sub-ensemble from Monte Carlo simulations which fits best to the experimental RDC and CS data is structurally very close to our reported excited state. The χ^2 function increases steeply with increasing RMSD to the starting structure (Fig. S19B), in-turn showing that as we move away from our current model of the excited state, the agreement between fit and experimental CS and RDCs quickly becomes much poorer. There is also an approximately linear correlation between χ^2_{RDC} and χ^2_{CS}, showing that both the RDC and CS data consistently point to the same excited state structure, which is structurally resembles the CS-Rosetta model.

Next, we sought to generate ensembles of $CytR^N$ where the α-helices fluctuate less than during the Monte Carlo simulations, to determine whether small changes in helix orientation can provide better agreement to the RDC and CS data than the current excited state fit. In order to derive this ensemble, we carried out all-atom molecular dynamics simulations for a total time of 200 ns starting from the current structure of the excited state. 20000 structures were generated and the experimental CS and RDC data were fit to each of these 20000 structures to evaluate the goodness-of-fit χ^2 function.

Figure S20A shows the 10 members of the MD ensemble that fit best to the experimental RDCs and CS. All 10 structures closely resemble the CS-Rosetta model, with all-atom RMSDs varying between 0.6 and 1 Å with the starting structure (the CS-Rosetta structure equilibrated in the MD water bath, which has an all-atom RMSD of 0.3 Å to the excited state structure and a χ^2 = 441). As with the Monte Carlo sampling, a convergence funnel is seen with the MD

structures also (Fig. S20B), where the goodness-of-fit improves as the RMSD decreases and the structures approach the CS-Rosetta structure. Notably, none of the MD-generated conformations agrees better with the input CS and RDCs than the starting structure.

Taken together, ensembles generated by Monte Carlo sampling and all-atom simulations do not agree better with the experimental CS and RDC data than the CS-Rosetta model of the excited state, indicating that the CS-Rosetta structure is a reliable model for the experimental measurements.

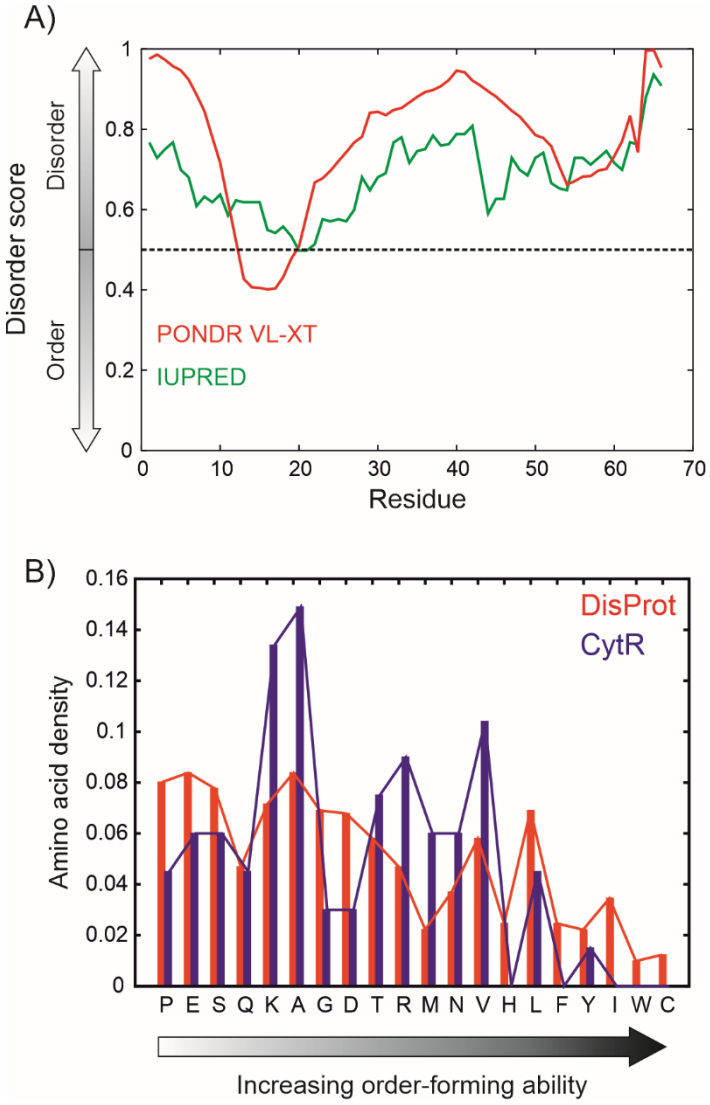

Fig. S1.

$CytR^N$ is predicted to be intrinsically disordered. A) Residue-specific disorder scores calculated using the PONDR VL-XT (*29*, *30*) algorithm (red) and IUPRED (*31*) (green). B) Bar plot of the probability of occurrence of each of the 20 amino acids in $CytR^N$ (blue), arranged according to their increasing order-forming tendency. (Red) The frequency of each amino acid in the DisProt database (*100*) of intrinsically disordered proteins.

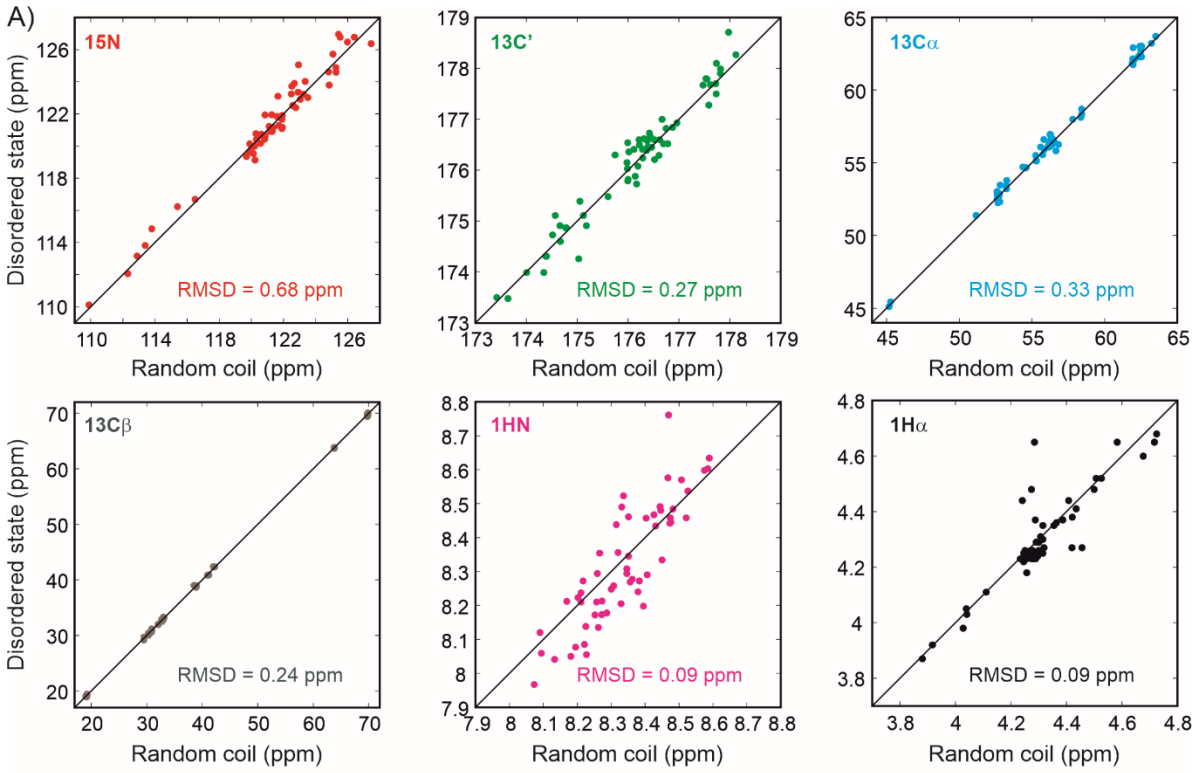
A)
15N
RMSD = 0.68 ppm
13C'
RMSD = 0.27 ppm
13Cα
RMSD = 0.33 ppm
13Cβ
RMSD = 0.24 ppm
1HN
RMSD = 0.09 ppm
1Hα
RMSD = 0.09 ppm
Disordered state (ppm)
Random coil (ppm)

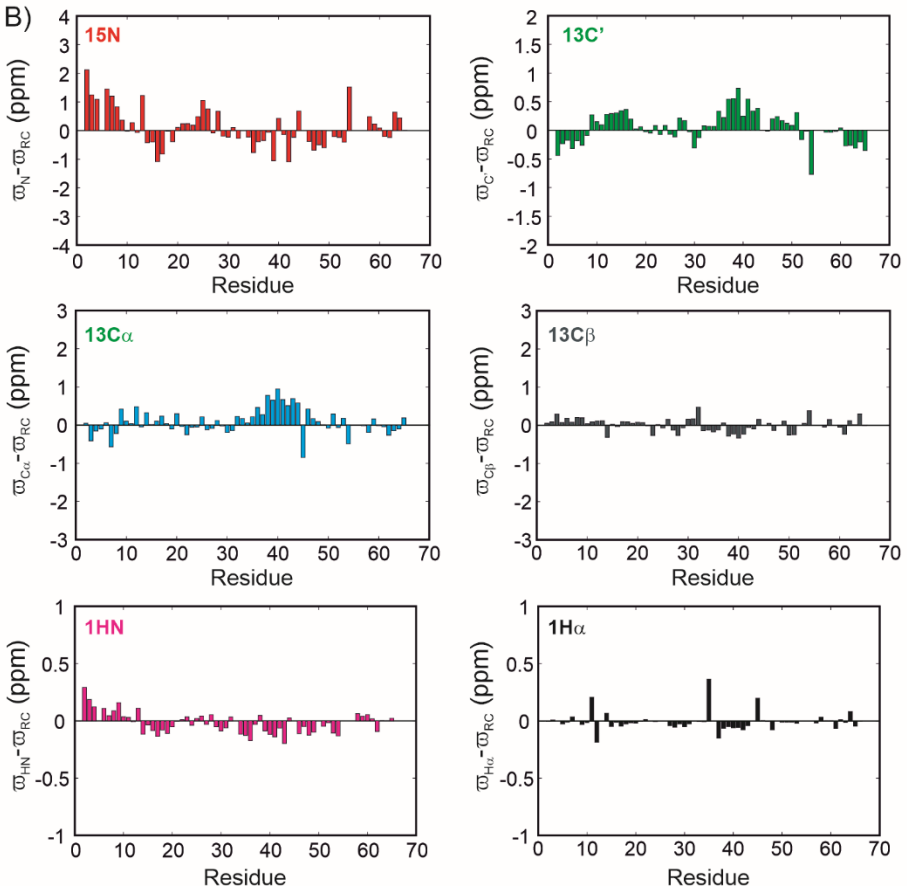
B)
15N
13C'
13Cα
13Cβ
1HN
1Hα
Residue

Fig. S2.

NMR backbone chemical shifts confirm that $CytR^N$ is intrinsically disordered. A) Correlation between random coil chemical shifts for $CytR^N$ (*101*) and the NMR backbone chemical shifts for disordered $CytR^N$. Solid lines in each panel are graphs of the y=x function. B) Residue-specific secondary chemical shifts for backbone nuclei of $CytR^N$ in the disordered state plotted as the difference between the NMR chemical shift and the corresponding random coil value.

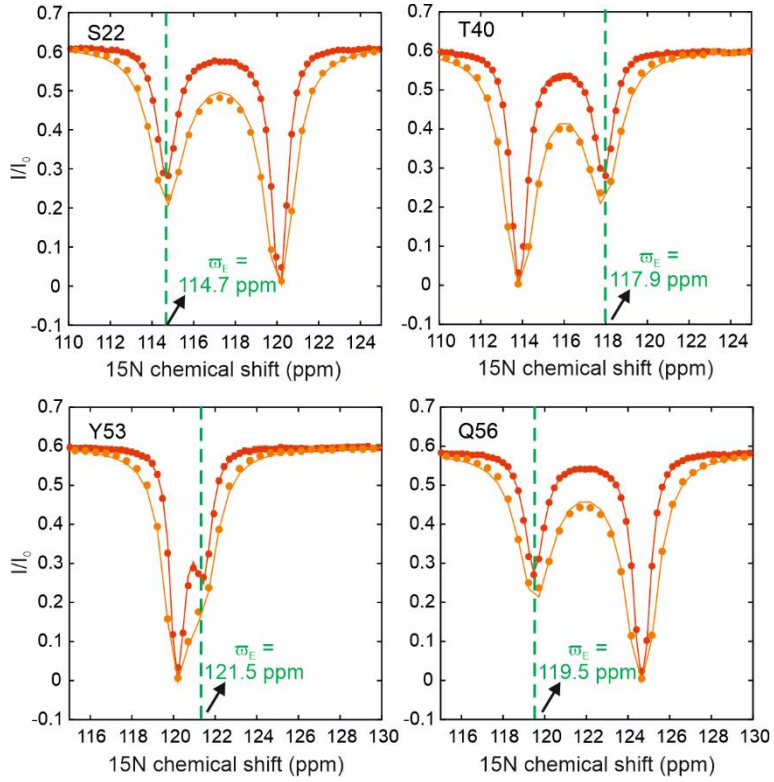

Fig. S3.

^{15}N CEST profiles of wt CytR^{N} reveal the presence of a conformationally excited state. ^{15}N CEST profiles of S22, T40, Y53 and Q56 acquired at 14.7 Hz (red) and 28.6 Hz (orange). Solid lines are global fits of the CEST data to the Bloch-McConnell equations for two-site exchange, while the dashed line shows the chemical shift position of the excited state.

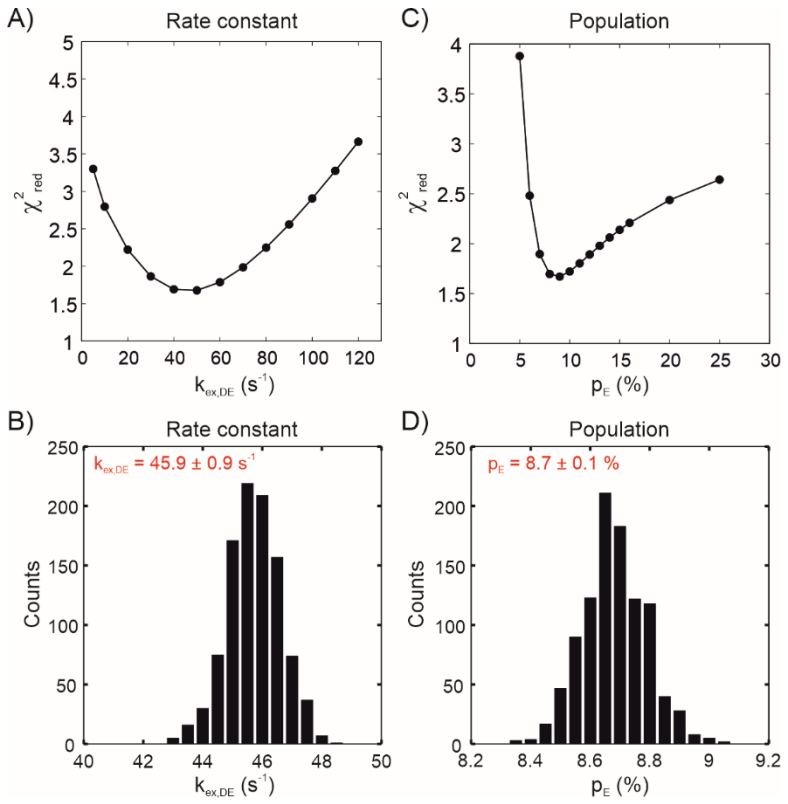

Fig. S4.

χ^2_{red} surfaces (A,C) and Monte Carlo distributions (B,D) for the exchange rate constant between the disordered and excited state ($k_{ex,DE}$; A,B) and the population of the excited state (p_E; C,D) obtained from fitting ^{15}N CEST data acquired on Sample 1.

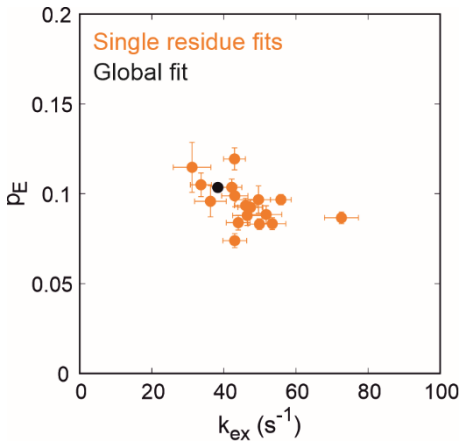

Fig. S5.

p_E and $k_{ex,DE}$ values from single residue fits (orange) of 2 B_1 field ^{15}N CEST data acquired on $CytR^N$ (Sample 1) cluster closely around the value from the global fit (black).

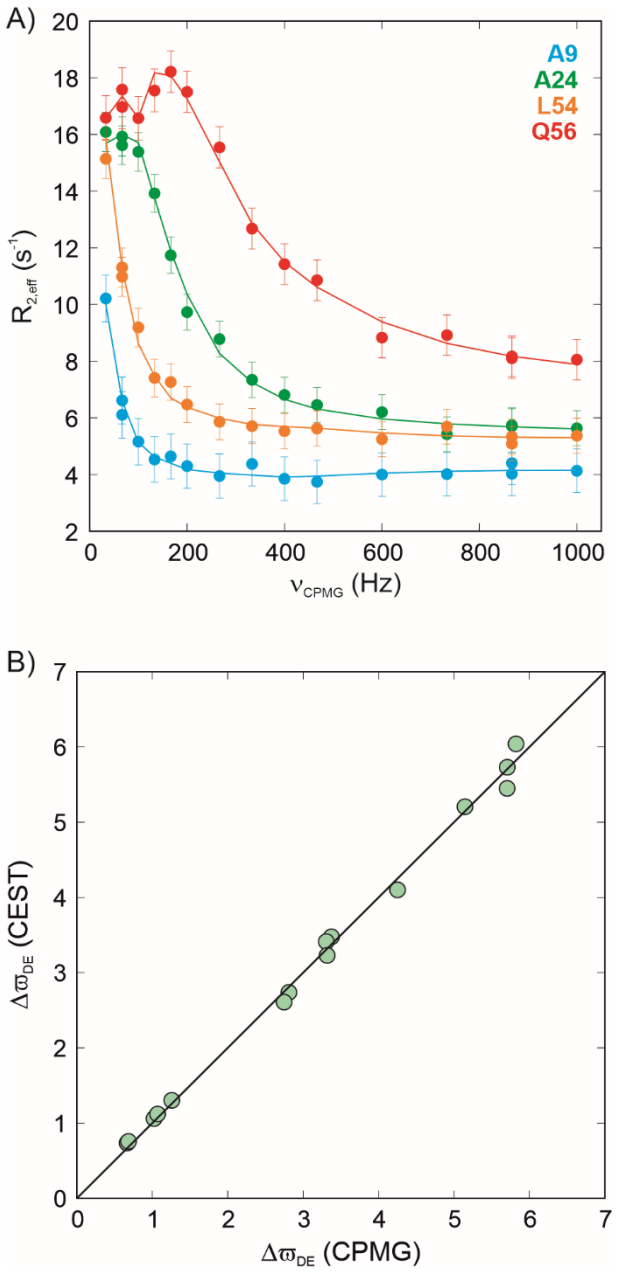

Fig. S6.

^{15}N CPMG data confirm the presence of an excited state in equilibrium with disordered CytR^{N}. A) ^{15}N CPMG profiles for four residues acquired on CytR^{N} (Sample 2) at 287 K on an 800 MHz spectrometer. Data for 16 residues at 2 B_0 fields (700 MHz and 800 MHz) were fit together to extract p_E and $k_{ex,DE}$ values. B) Correlation plot of the magnitudes of chemical shift differences between the disordered and excited states ($\Delta\varpi_{DE}$) obtained from ^{15}N CPMG (x-axis) and CEST experiments (y-axis), showing a very good agreement between the two values, indicating that both experiments are reporting on the same excited state.

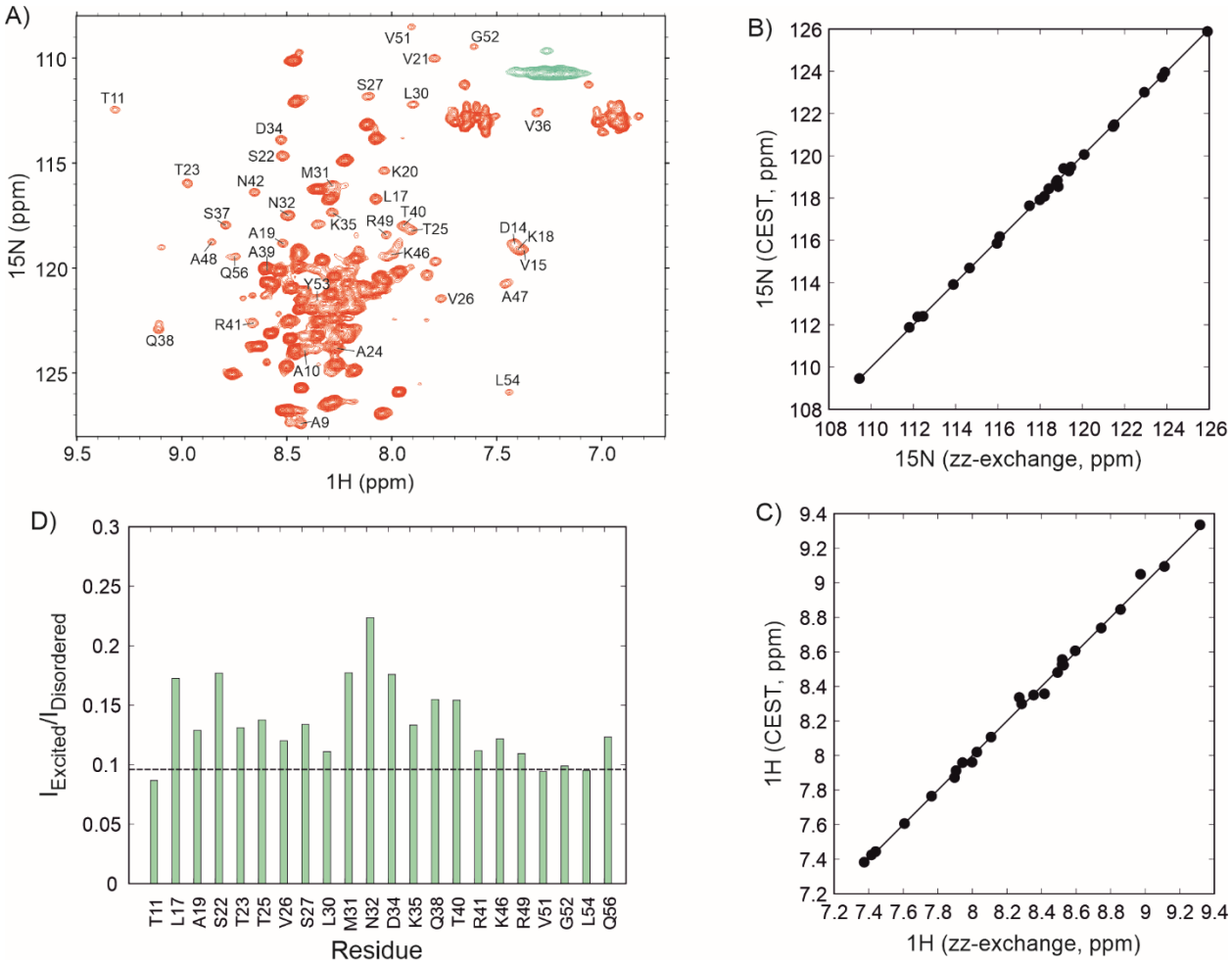

Fig. S7.

The excited state of CytR^{N} can be directly observed at low contour levels in ^{1}H-^{15}N HSQC spectra. A) ^{1}H-^{15}N HSQC spectrum of CytR^{N} plotted at low contour levels. A second set of weak peaks originating from the excited state are labeled with their corresponding residue-specific assignments. Magnetization exchange experiments (Fig. 2C) were used to assign peaks from the second state observed in the HSQC spectrum (panel A) and the assignments for the second state are indicated next to each peak in panel A. B,C) Correlation plots for ^{15}N and ^{1}H chemical shifts of the excited state derived from CEST experiments with the shifts obtained from HSQC spectra. The correlation is very good, confirming that the second set of resonances observed at low contour levels in the HSQC spectrum originate from the same excited state seen in CEST profiles. D) Residue-specific ratios of the excited to disordered state peak intensities. The expected value from ^{15}N CEST experiments is indicated as a black dashed line. All experiments in this figure were acquired on Sample 1.

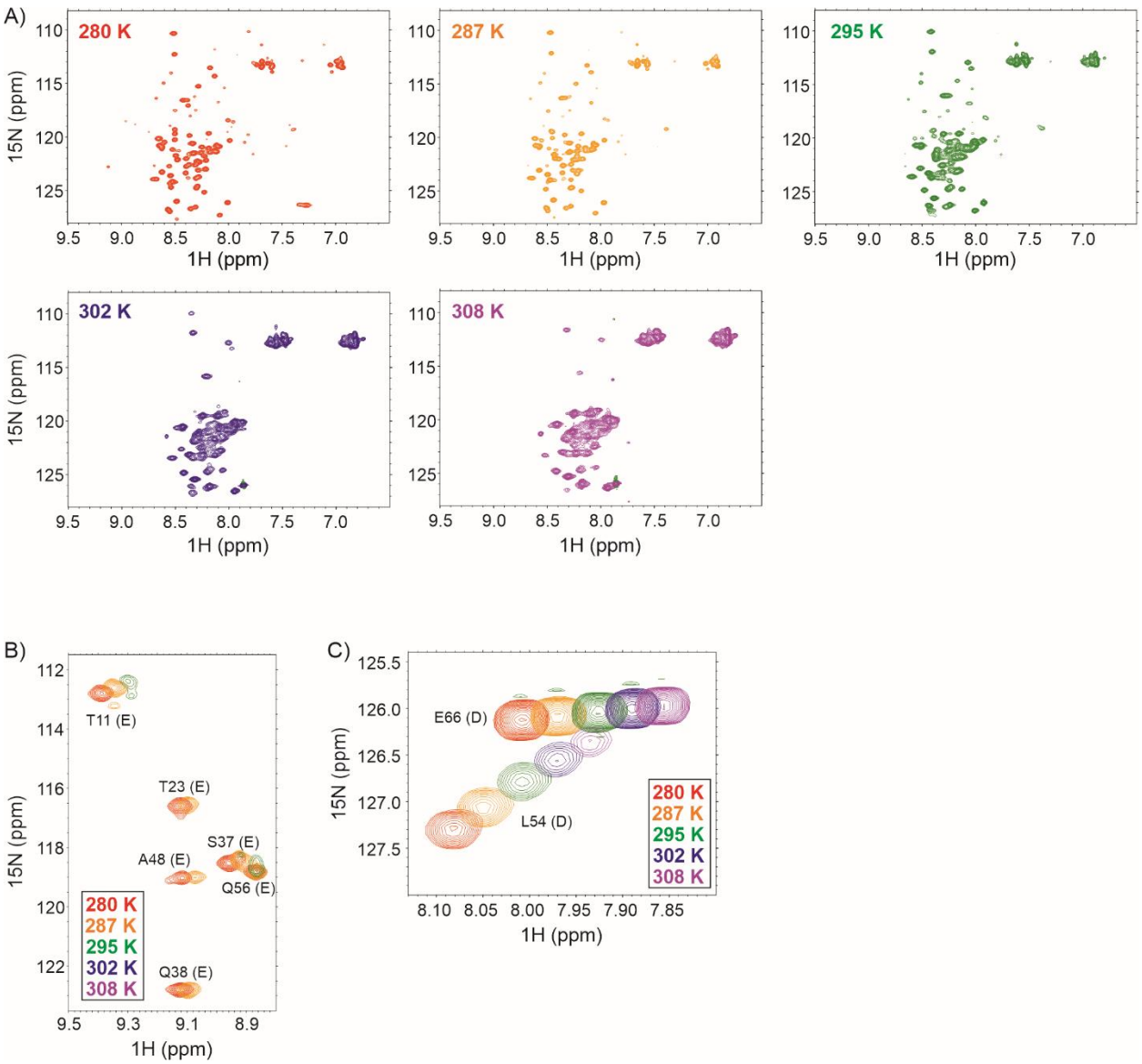

Fig. S8.

The disordered state of CytR^{N} is not a cold-denatured state. A) ^{1}H-^{15}N HSQC spectra of CytR^{N} acquired at temperatures ranging from 280 – 308 K indicating that the disordered state is the major state at all the temperatures. B,C) Overlays of the HSQC spectra at different temperatures showing changes in excited (E) or disordered (D) peak intensities with temperature.

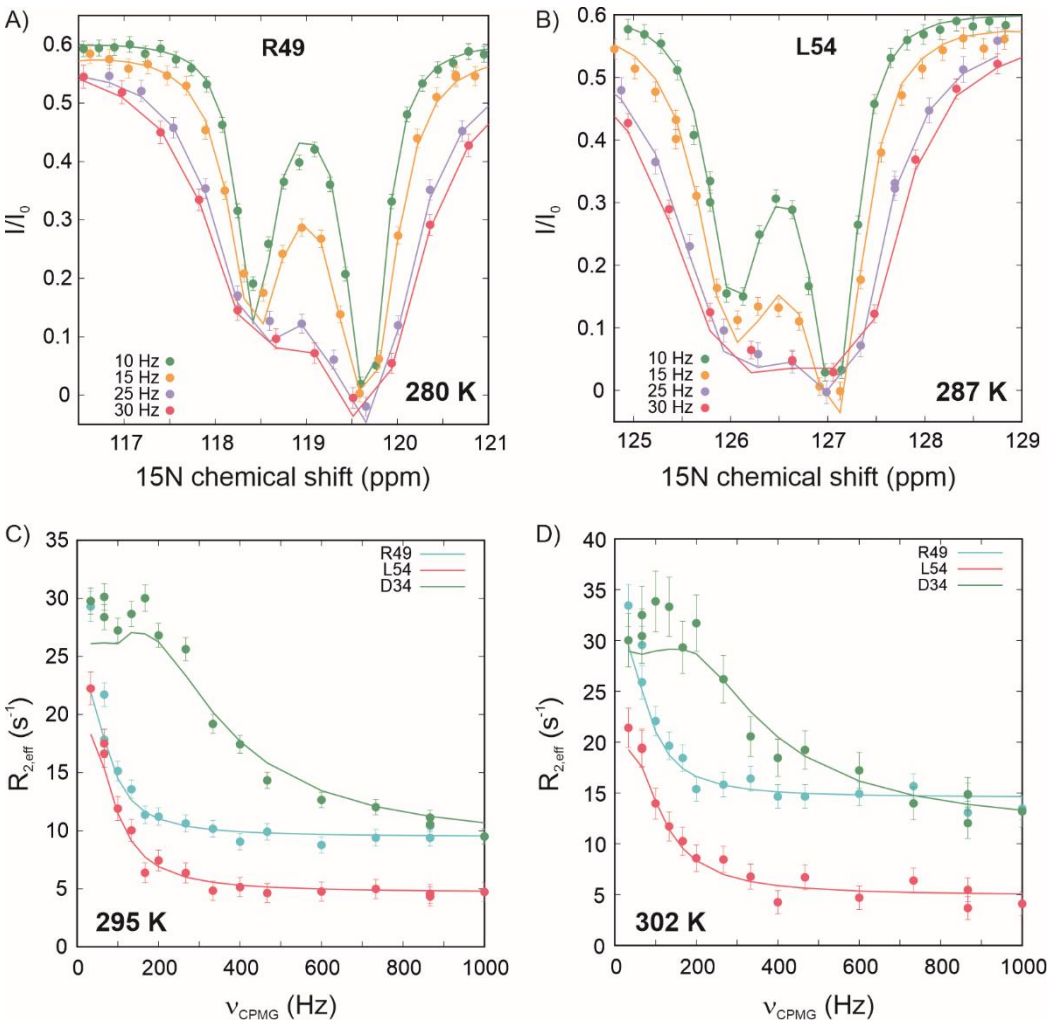

Fig. S9.

Measuring p_E and $k_{ex,DE}$ as a function of temperature. ^{15}N CEST profiles acquired at (A) 280 K and (B) 287 K, and ^{15}N CPMG profiles acquired at (C) 295 K and (D) 302 K. All variable temperature data were acquired on Sample 2.

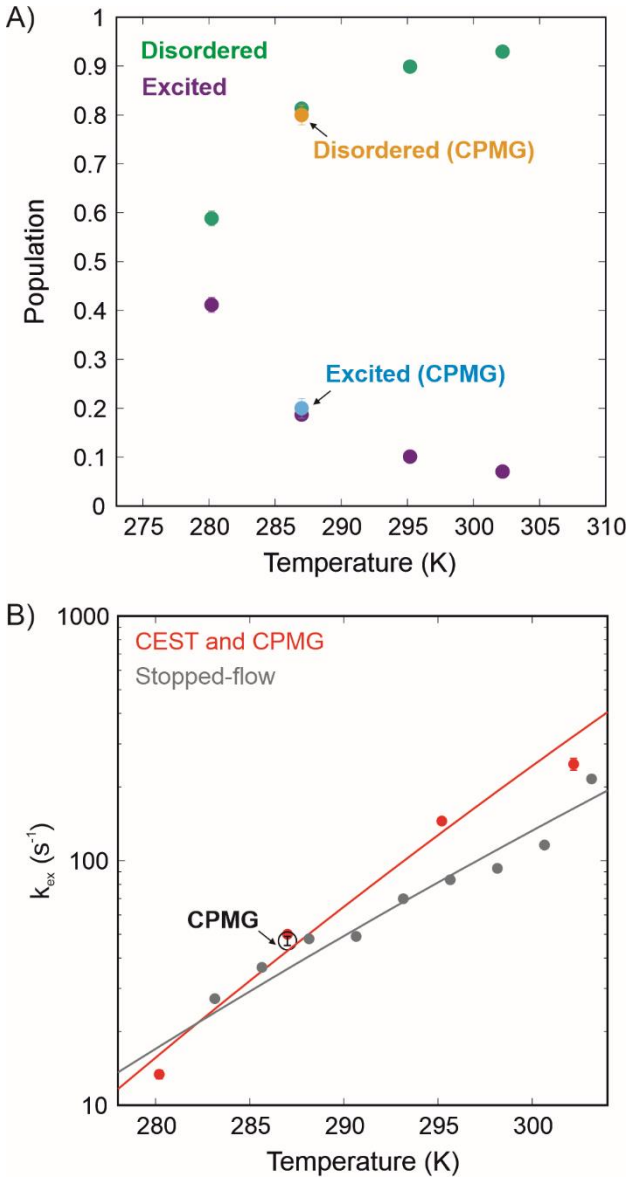

Fig. S10.

Temperature dependencies of p_E and $k_{ex,DE}$ determined from ^{15}N CEST and CPMG experiments. A) Population of the disordered (green) and excited states (purple) as a function of temperature. ^{15}N CPMG experiments at 287 K and 2 B_0 field strengths (700 MHz and 800 MHz) were fit separately and the corresponding populations are shown as orange (disordered) and cyan (excited) circles. B) $k_{ex,DE}$ values obtained by fitting ^{15}N CEST and CPMG data shown as red filled circles. Exchange rate constant measurements from fluorescence-detected stopped-flow experiments (*35*) are shown as grey filled circles. Solid lines are fits of the corresponding data to an exponential Arrhenius function. The $k_{ex,DE}$ value obtained from a separate fit of the ^{15}N CPMG data at 287 K and 2 B_0 field strengths is shown as a black open circle. All data for this figure were obtained on Sample 2. At 280 K and 287 K, 4 B_1 field CEST data were globally fit at each temperature to extract p_E and $k_{ex,DE}$ values, while ^{15}N CPMG profiles at 700 MHz

were globally fit in concert with 6 B_1 field and 3 B_1 field ^{15}N CEST data at 295 K and 302 K respectively.

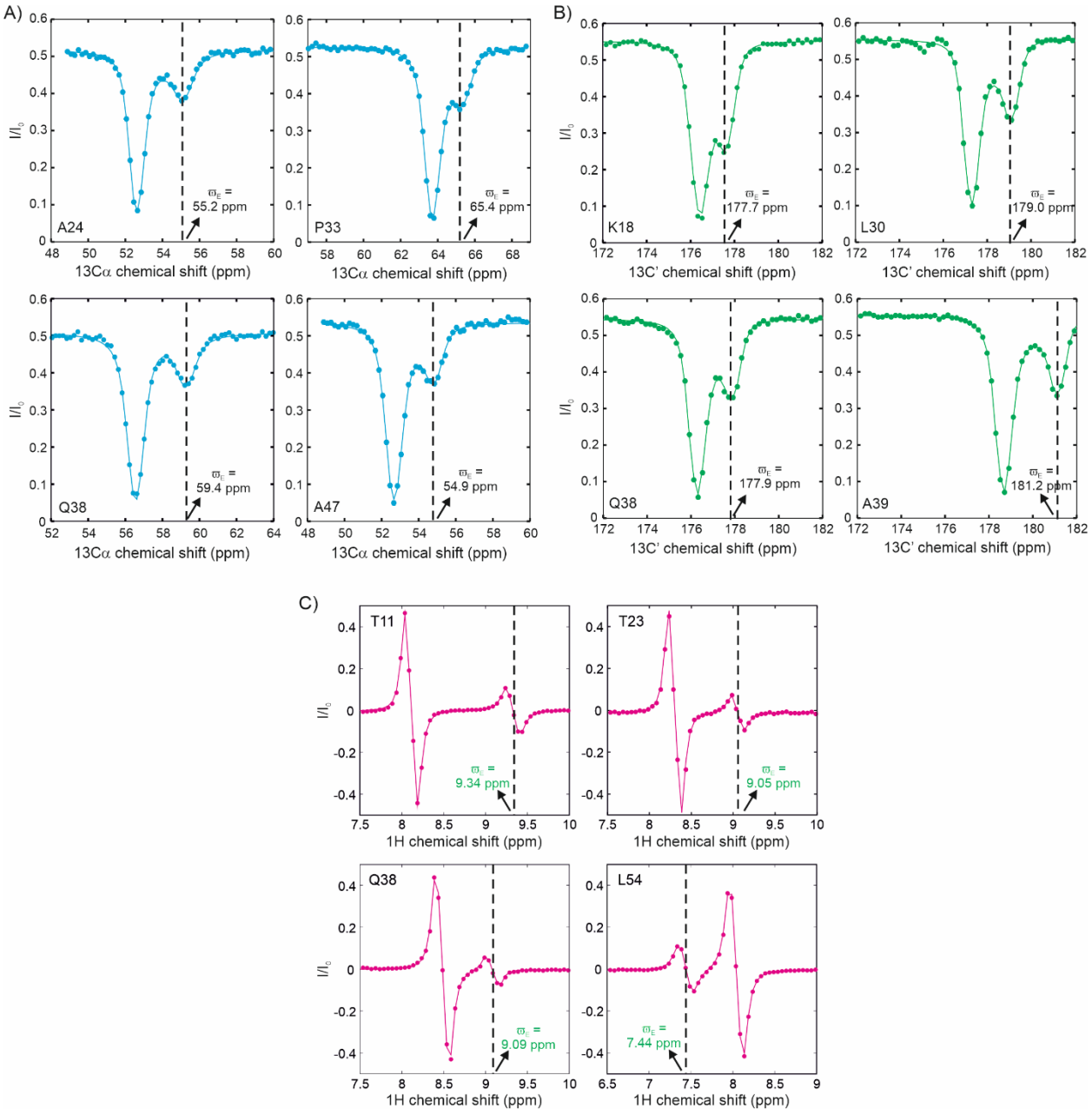

Fig. S11.

A) $^{13}C\alpha$, B) $^{13}C'$ and C) $^{1}H^{N}$ CEST profiles showing the exchange between the disordered native ensemble and the excited state of $CytR^{N}$. The dashed line shows the chemical shift position of the excited state.

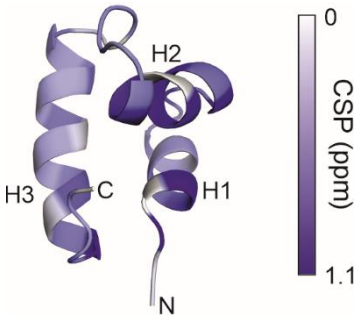

Fig. S12.

Cartoon representation of the three-helix bundle structure of DNA-bound $CytR^N$ (PDB ID: 2LCV (*33*)). The backbone has been coloured from white to purple according to the magnitude of the chemical shift perturbation (CSP) of each residue between the disordered and excited state. The color bar mapping the colour with the CSP value is shown alongside.

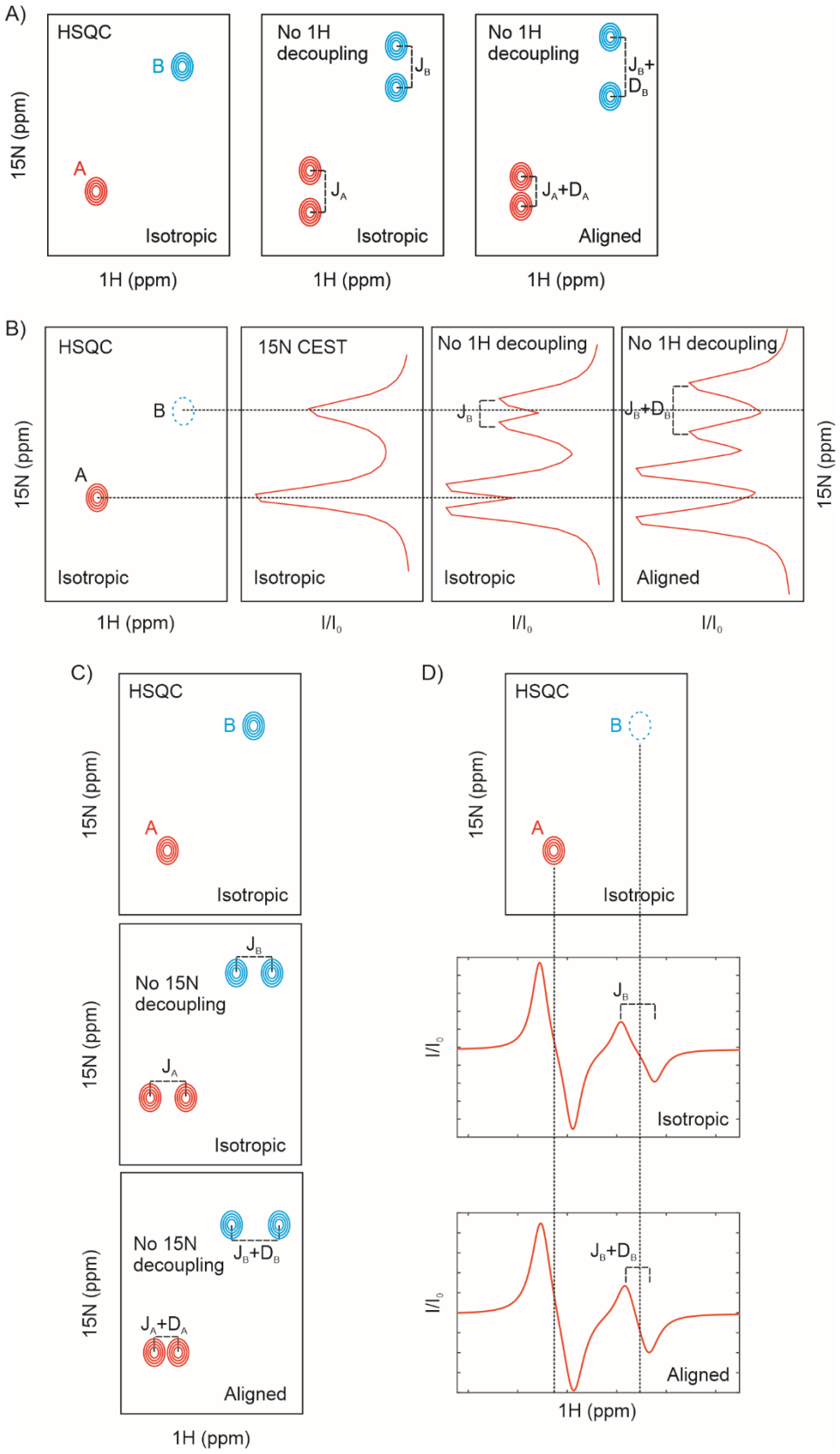

Fig. S13.

Schematic of how excited state RDC measurements were made using ^{15}N and $^{1}H^{N}$ CEST profiles. A,C) $^{1}H^{N}$-^{15}N RDCs for a protein exchanging between two visible conformations A

and B can be measured by removing either $^{1}H^{N}$ decoupling during t_1 (A) or ^{15}N decoupling during t_2 from a heteronuclear correlation NMR experiment. The splitting between the doublets in an isotropic sample (middle panel) gives $^{1}J_{NH}$, while the splitting in an aligned sample gives $^{1}J_{NH}$+RDC (panel A, right; panel C, bottom), with the difference corresponding to the residue-specific RDC value. (B,D) ^{15}N and $^{1}H^{N}$ CEST profiles can be used to visualize the excited state B which is not observable in heteronuclear correlation spectra and also to determine the RDC values for both states A and B. In the ^{15}N CEST experiment (panel B), the major state A and the minor state B both give rise to dips in intensity in an isotropic sample. If the ^{1}H decoupling during the exchange duration is removed, each dip splits into a doublet separated by $^{1}J_{NH}$ in the isotropic sample and $^{1}J_{NH}$+RDC in the aligned sample. In the $^{1}H^{N}$ CEST experiment the CEST profile is already a difference of two Lorentzians, one corresponding to the TROSY component (H_zN_β) and the other to the anti-TROSY component (H_zN_α). Therefore, the lineshape contains information about $^{1}J_{NH}$ in the isotropic sample and $^{1}J_{NH}$+RDC in the aligned sample.

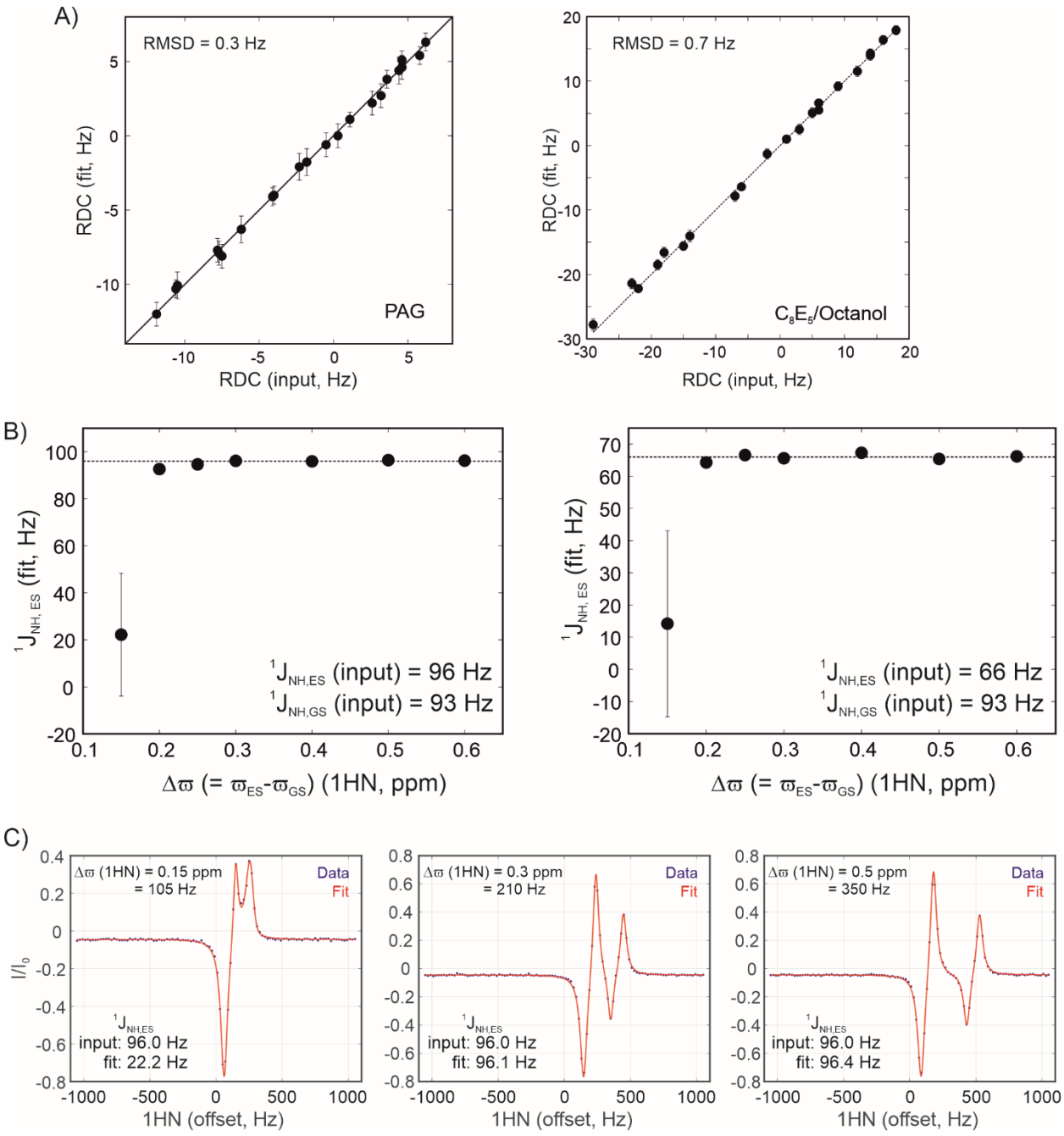

Fig. S14.

^{1}H-^{15}N backbone amide RDCs can be estimated robustly using $^{1}H^{N}$ CEST profiles. A) Correlation plot between input RDCs (x-axis) and RDCs obtained by fitting simulated $^{1}H^{N}$ CEST profiles (y-axis, Supplementary Text). Input RDCs are based either on experimental values measured in PAG (left panel) or C_8E_5/octanol (right panel). B) $^{1}J_{NH,ES}$ values extracted from fits of $^{1}H^{N}$ CEST profiles for varying values of $\Delta\varpi_{DE}$. The input $^{1}J_{NH,ES}$ is either 96 Hz (left panel) or 66 Hz (right panel), while $^{1}J_{NH,GS}$ is the same in both panels (93 Hz). C) Simulated $^{1}H^{N}$ CEST profiles (blue circles) for $\Delta\varpi_{DE}$ = 0.15 ppm (left), 0.3 ppm (middle) and

0.5 ppm (right). Fits of the profiles to sums of Lorentzians are shown as red lines. Input $^{1}J_{NH,ES}$ and values generated by the fitting routine are indicated on the plot.

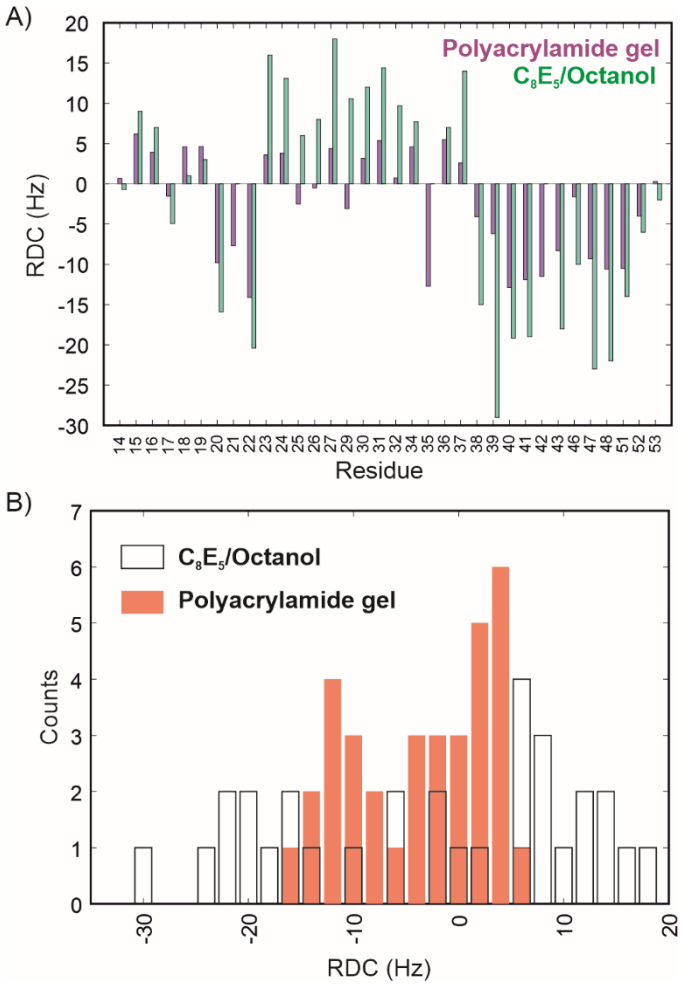

Fig. S15.

A) Bar plot of experimentally measured excited state RDCs (aligned – isotropic) in PAG (green) and C_8E_5/octanol (purple). B) Histogram of experimentally measured RDCs in PAG (filled orange boxes) and C_8E_5/octanol (open boxes).

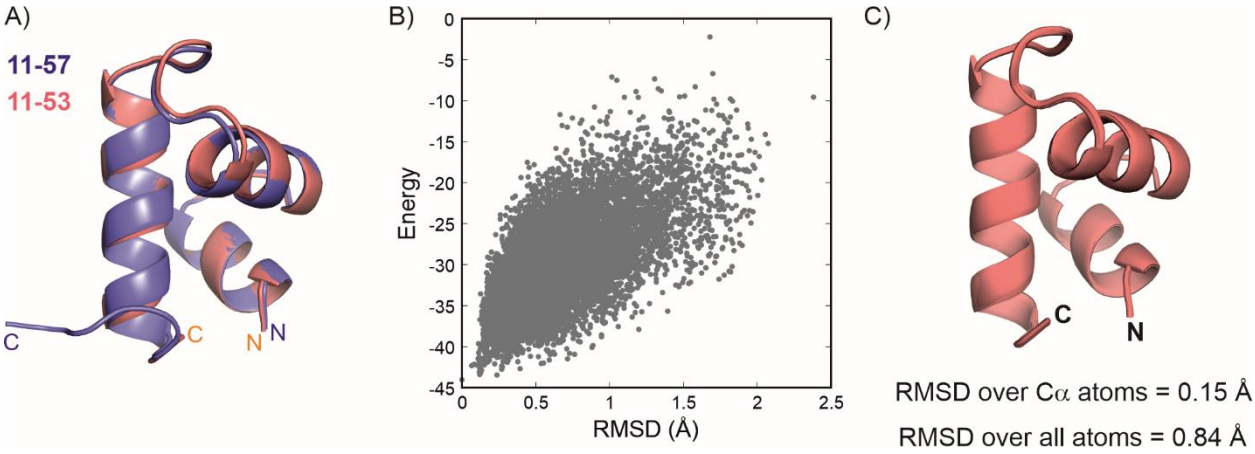

Fig. S16.

A) Comparison of the CS-Rosetta structures of CytR^{N}(11-53) (red) and CytR^{N}(11-57) (blue), showing that the three-helix bundle topology is identical in both structures and that the residues from 54-57 do not adopt any specific secondary structure. B) Plot of the energies of the 10000 conformations sampled during the CS-Rosetta structure calculation against the RMSD of each structure with the lowest energy conformation. C) Superposition of the 10 lowest energy conformations generated by CS-Rosetta.

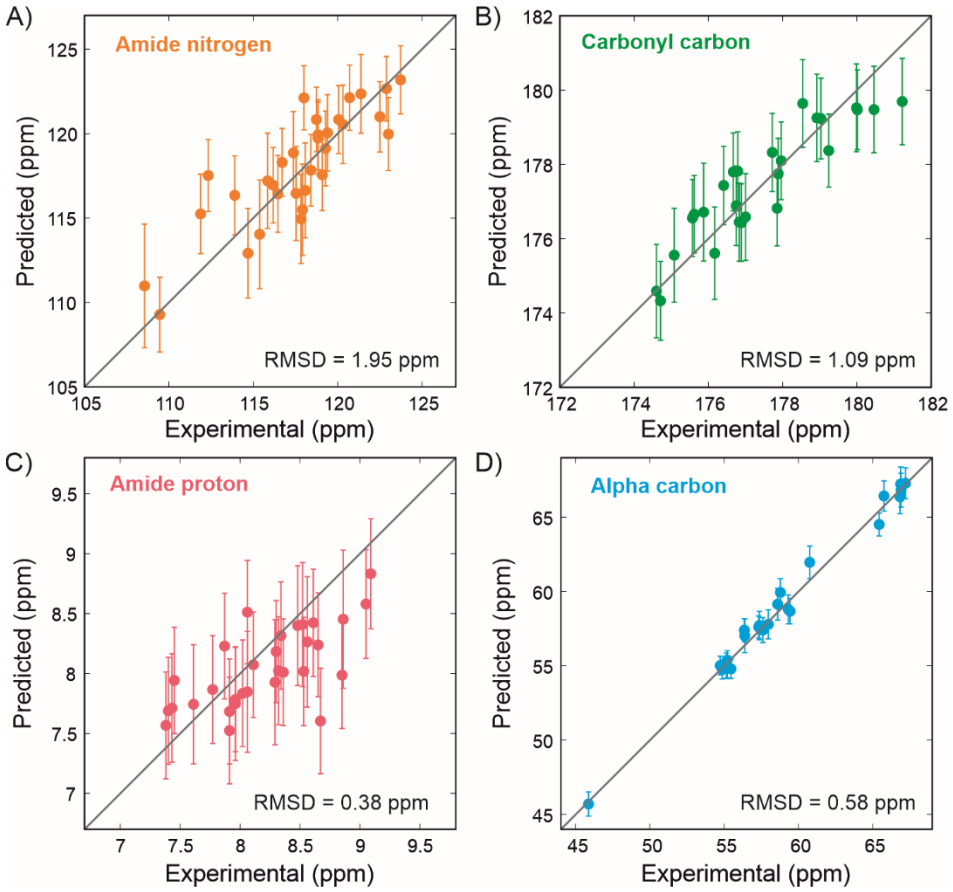

Fig. S17.

A comparison of the experimental ^{15}N (A), $^{13}C'$ (B), $^{1}H^{N}$ (C) and $^{13}C\alpha$ (D) chemical shifts (x-axis) with the shifts predicted by Sparta+ for the lowest energy conformer from CS-Rosetta (y-axis). The RMSD values for each correlation are indicated on the plot in ppm. The errors in the predicted chemical shifts are obtained directly from Sparta+.

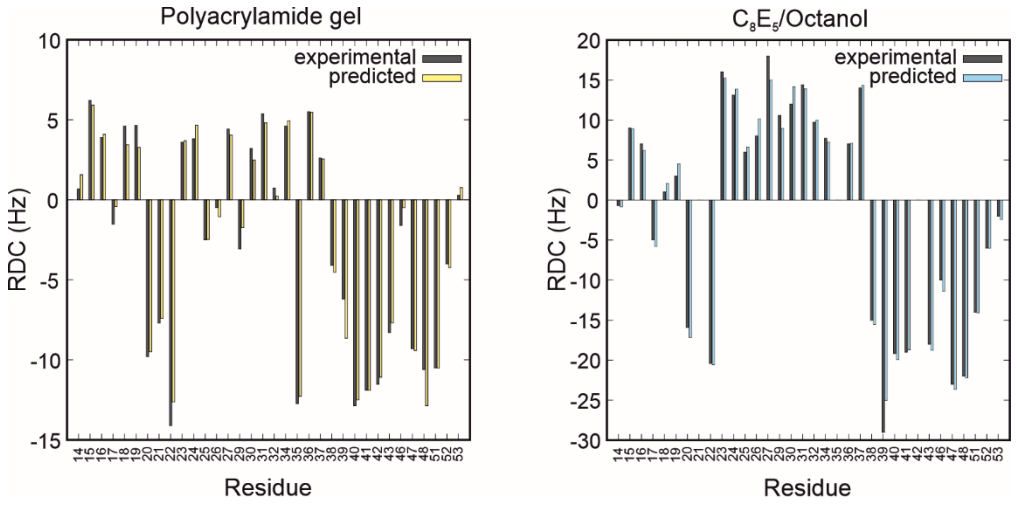

Fig. S18.

Bar plots of experimental (black) and back-predicted RDCs (yellow in the left panel and blue in the right panel) for PAG (left) and C_8E_5/octanol (right). All RDCs are calculated as $^1J_{NH}$(aligned) – $^1J_{NH}$(unaligned). RDCs were back-predicted for the lowest energy CS-Rosetta conformer using PALES (see Materials and Methods).

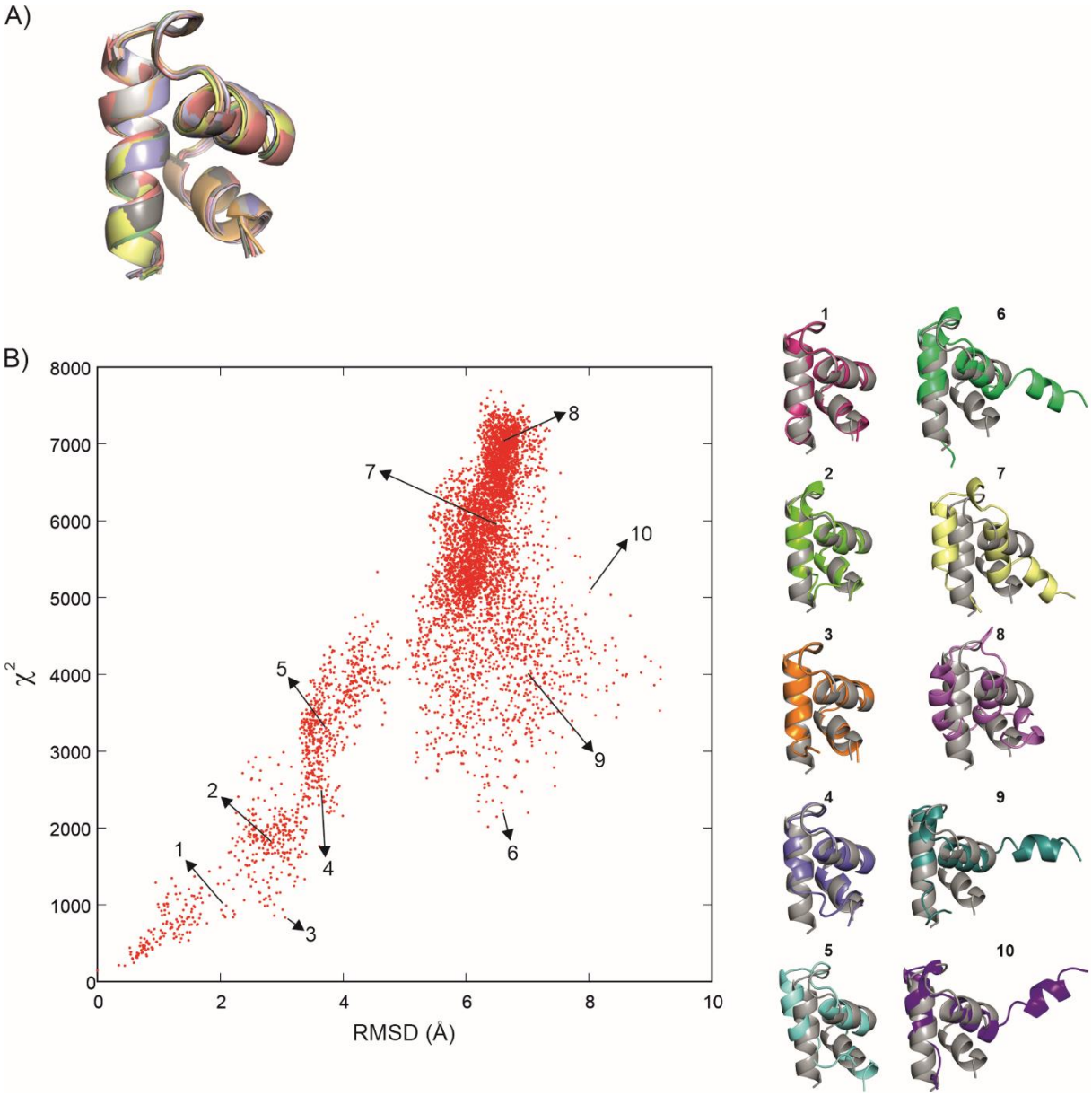

Fig. S19.

A) Overlay of the 10 structures selected from Monte Carlo sampling that fit best to the experimental chemical shift and RDC data. B) χ^2 values depicting the goodness-of-fit of conformations sampled by the Monte Carlo algorithm to the chemical shift and RDC data plotted against the RMSD to the starting structure (also the CS-Rosetta based excited state structure, Fig. 3C). 10 conformations at specific points in the plot are shown on the right-hand side overlaid with the CS-Rosetta model in grey.

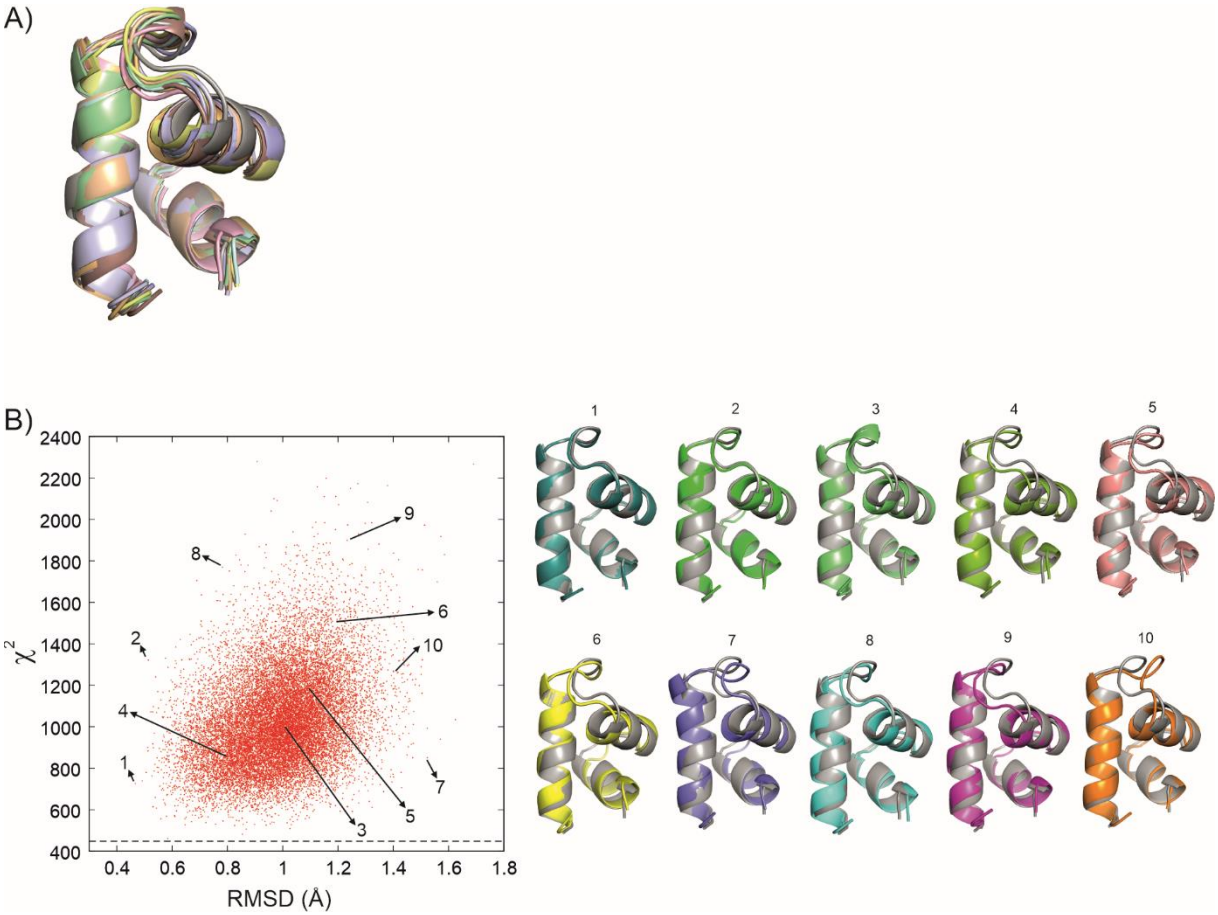

Fig. S20.

A) Overlay of the 10 structures selected from molecular dynamics simulations that fit best to the experimental chemical shift and RDC data. B) χ^2 values depicting the goodness-of-fit of conformations sampled during the MD simulations to the chemical shift and RDC data plotted against the RMSD to the starting structure (the CS-Rosetta model equilibrated in the MD water bath). 10 conformations at specific points in the plot are shown on the right-hand side overlaid with the CS-Rosetta model in grey.

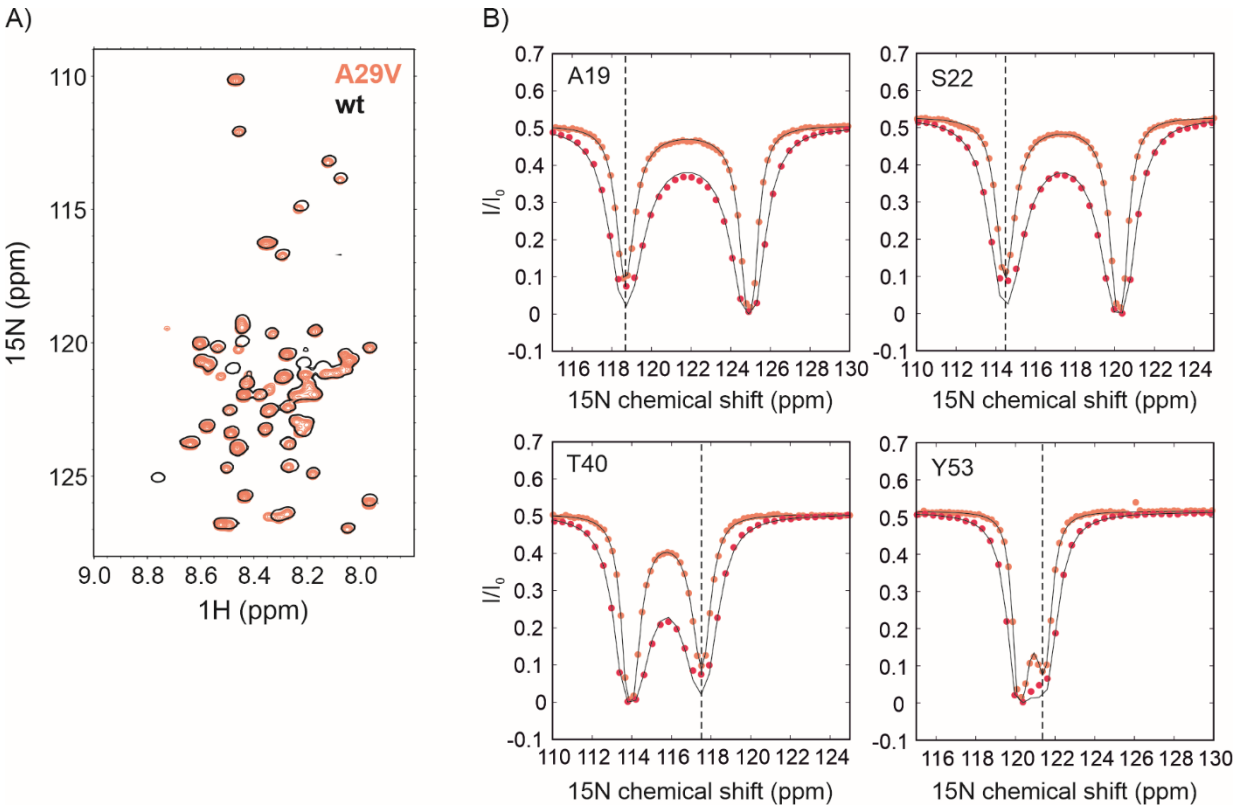

Fig. S21.

A) ^{1}H-^{15}N HSQC spectrum of A29V CytR^{N} (orange) overlaid with the spectrum of wt CytR^{N} (black). B) ^{15}N CEST profiles of A29V CytR^{N} acquired at 12.4 (orange) and 23.9 Hz (red). The black dashed line indicates the position of the excited state.

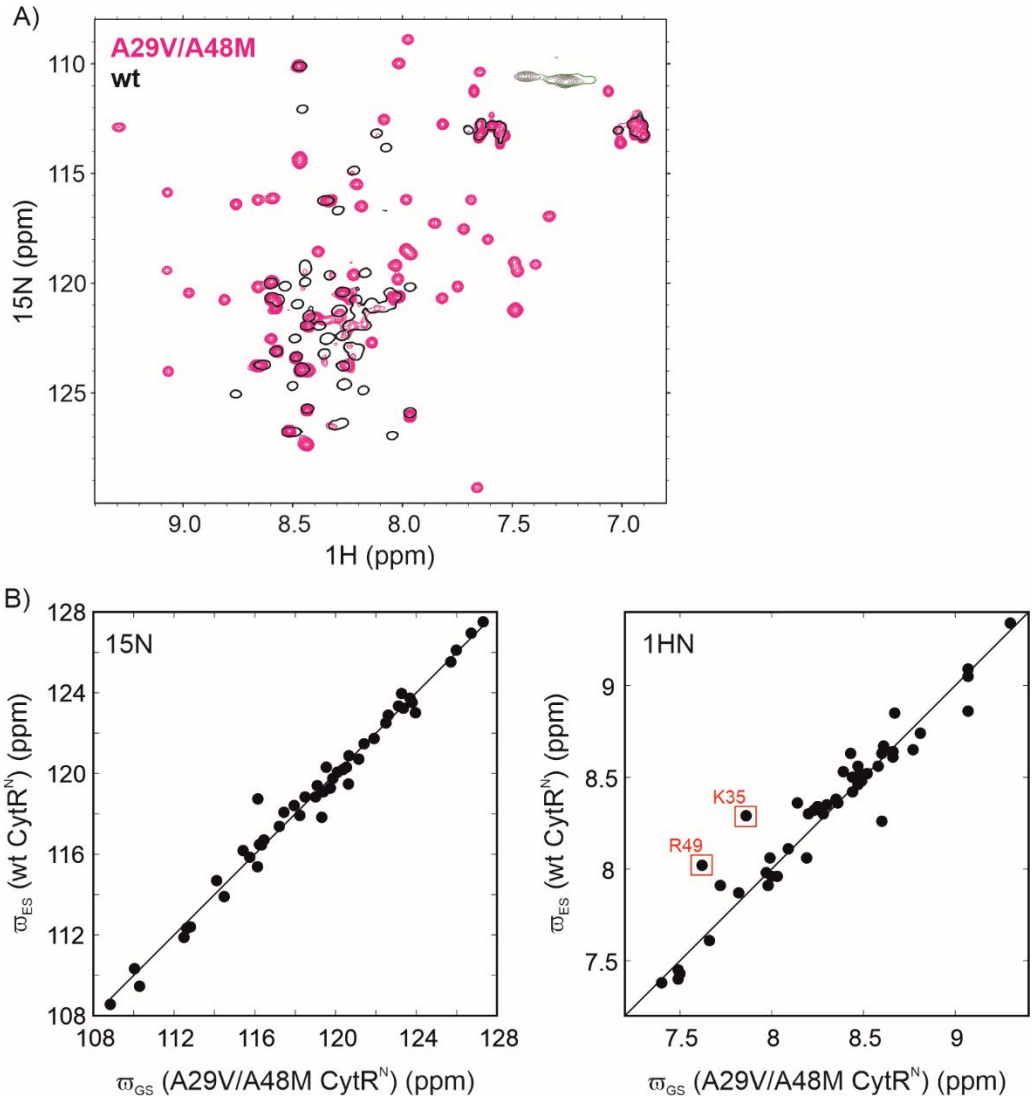

Fig. S22.

A) ^{1}H-^{15}N HSQC spectrum of A29V/A48M CytR^{N} (magenta) overlaid with the spectrum of wt CytR^{N} (black). The relative populations of the excited and ground states for A29V/A48M CytR^{N} were obtained directly from the ^{15}N-^{1}H HSQC spectrum, since resonances from both states were visible. Six isolated resonances for which reliable assignments could be obtained for both the excited and disordered conformations were used for analysis. The volumes of these peaks were used to determine the populations of the excited and disordered states. B) Correlations between the ^{15}N (left) and ^{1}H^{N} (right) chemical shifts of the folded ground state of A29V/A48M CytR^{N} (x-axis) and the excited state of wt CytR^{N} (y-axis). The solid line is a graph of the y=x function. R49 is adjacent to the site of A48M mutation, which likely results in the 0.4 ppm difference between the ^{1}H^{N} chemical shifts of the two states. K35 forms a hydrogen bond with N32 in excited state of wt CytR^{N}. The upfield shift of K35 ^{1}H^{N} chemical

shift by 0.4 ppm compared to wt $CytR^N$ suggests that this hydrogen bond is likely weakened or broken by the A29V mutation at the end of helix H2.

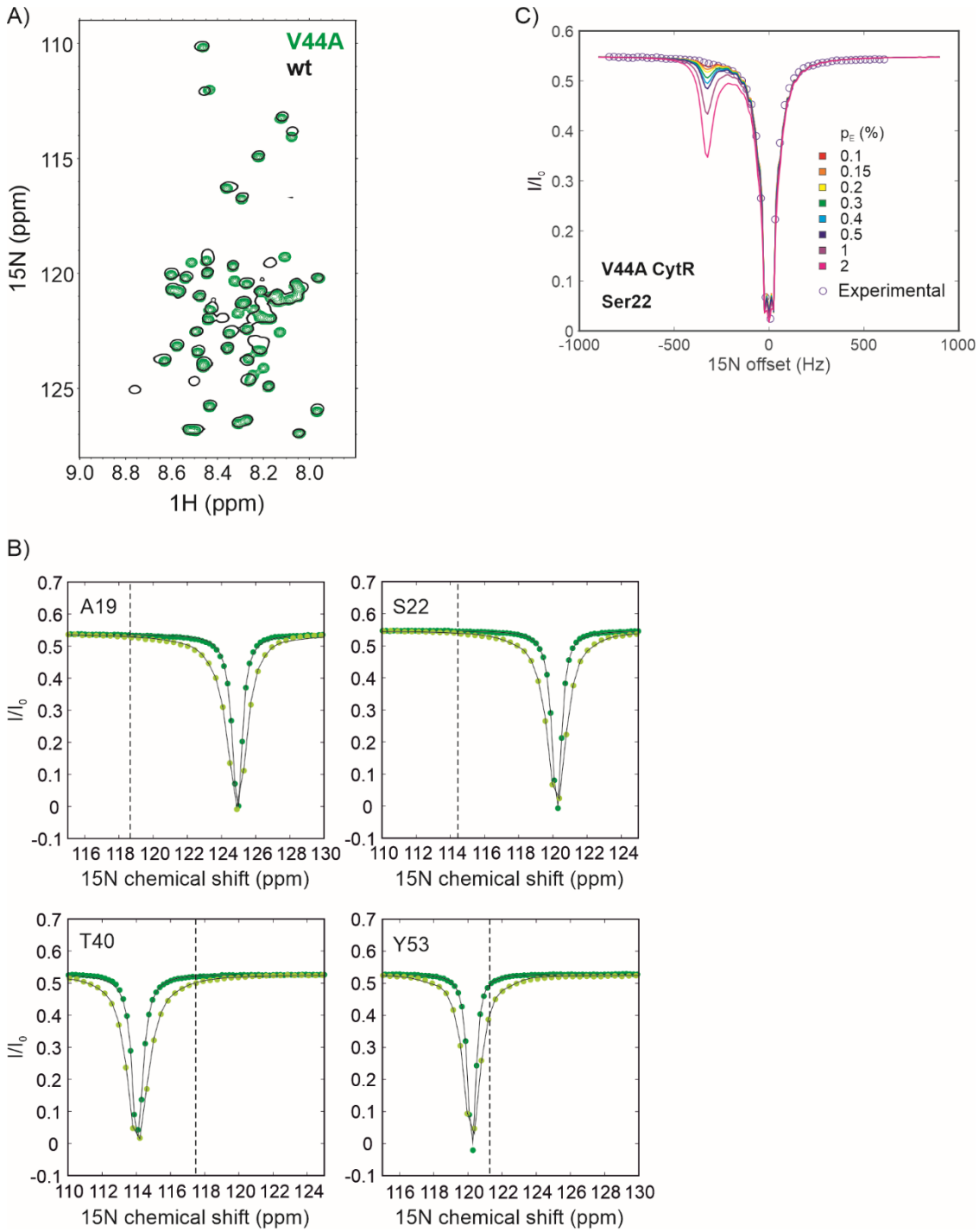

Fig. S23.

A) ^{1}H-^{15}N HSQC spectrum of V44A CytR^{N} (green) overlaid with the spectrum of wt CytR^{N} (black). B) ^{15}N CEST profiles of V44A CytR^{N} acquired at 14.0 (dark green) and 26.5 Hz (light green). The black dashed line indicates the position of the excited state. The minor dip at this position is absent in the CEST profiles of V44A CytR^{N}, confirming that the excited state is destabilized in this mutant. C) Obtaining the upper limit for the population of the excited state

for V44A CytR^{N}. Open circles indicate experimentally acquired ^{15}N CEST data (B_1 field of 26.5 Hz), while coloured lines are simulated CEST profiles for various populations ranging from 0.1 to 2 %. From the size of the minor dip, the upper limit of the population is estimated as 0.15 %, since minor dips for populations larger than 0.15 % are expected to be visible in CEST profiles of V44A CytR^{N}.

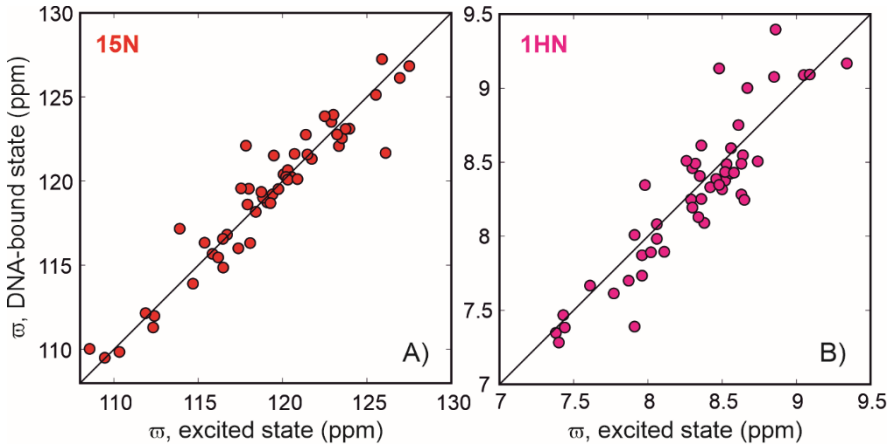

Fig. S24.

A comparison of ^{15}N (A) and $^{1}H^{N}$ (B) chemical shifts of the excited state (x-axis) and the DNA-bound state (y-axis) of $CytR^{N}$. Excited state chemical shifts were obtained from CEST profiles, while the shifts of the DNA-bound state are from BMRB ID 17419.

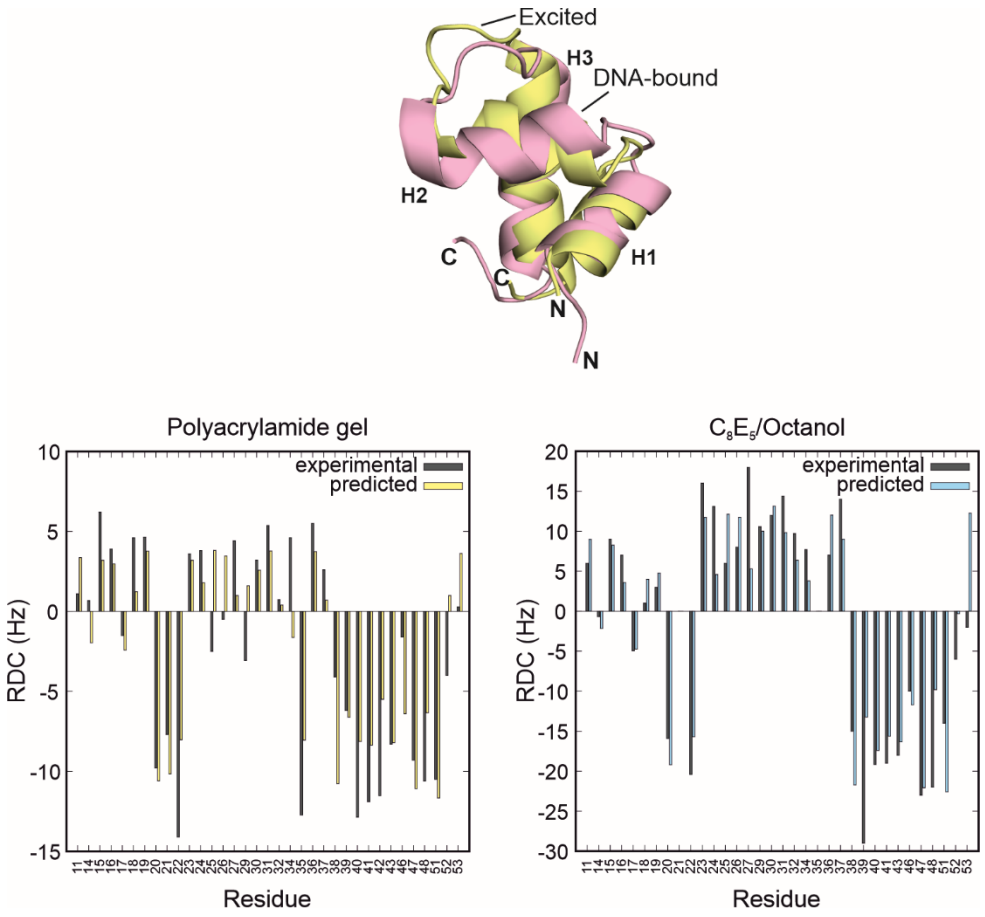

Fig. S25.

Fitting experimental excited state RDC data to the structure of DNA-bound CytR^{N}. (Top) Overlay of excited (yellow) and DNA-bound CytR^{N} (pink). (Bottom) Bar plots of experimental (black) and back-predicted RDCs (yellow in the left panel and blue in the right panel) for PAG (left) and C_8E_5/octanol (right).

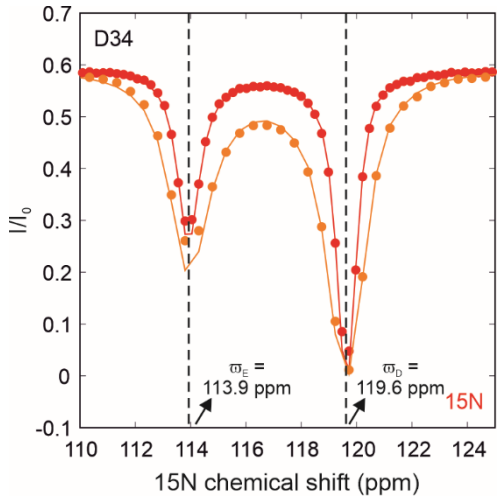

Fig. S26.

^{15}N CEST profiles of D34 acquired in absence of DNA at 14.7 (red) and 28.6 Hz (orange). The dashed black lines indicate the positions of the disordered and excited states at 119.6 and 113.9 ppm respectively.

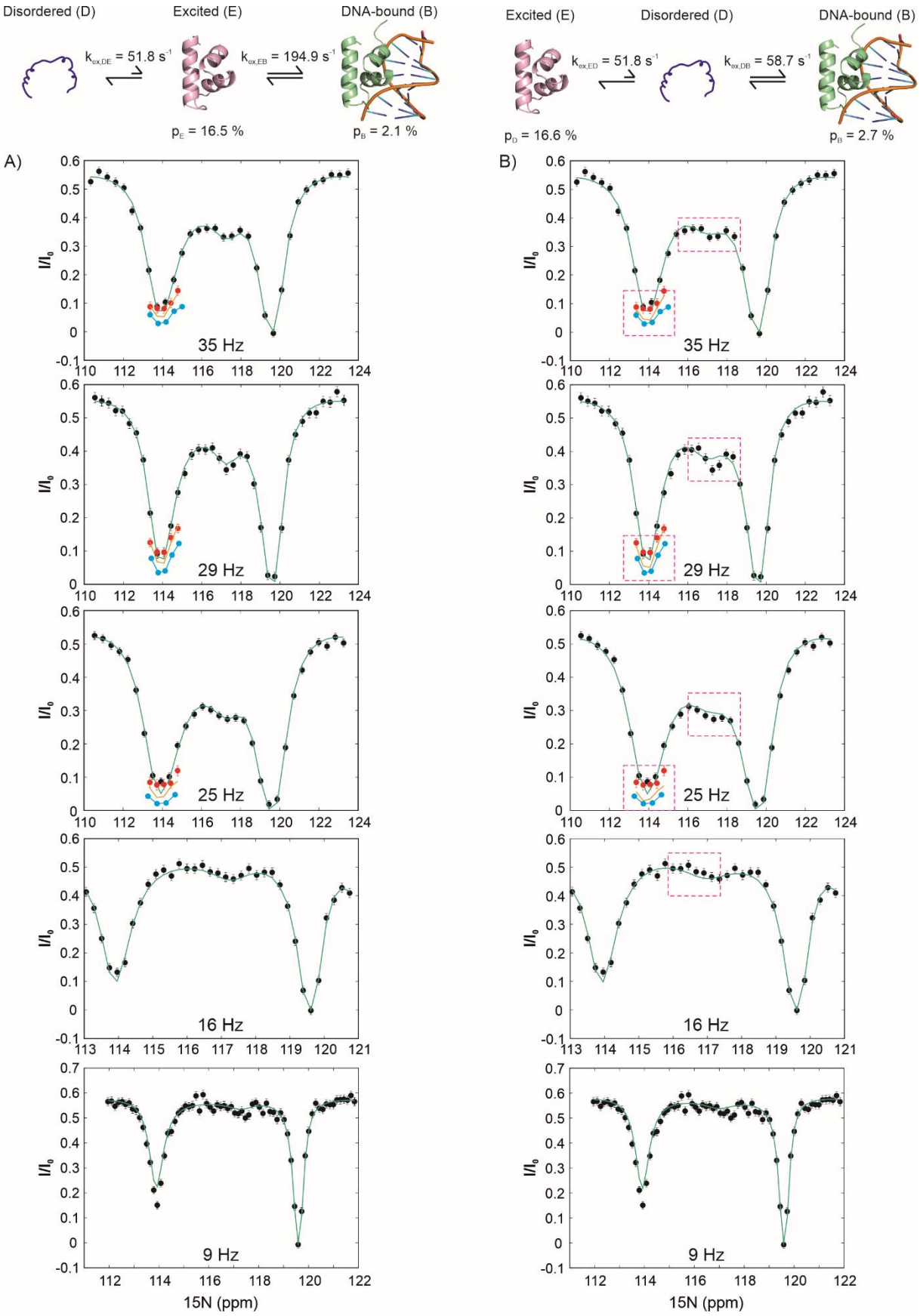
Disordered (D)
Excited (E)
DNA-bound (B)
$k_{ex,DE}$ = 51.8 s^{-1}
$k_{ex,EB}$ = 194.9 s^{-1}
p_E = 16.5 %
p_B = 2.1 %
A)
I/I0
35 Hz
29 Hz
25 Hz
16 Hz
9 Hz
15N (ppm)
Excited (E)
Disordered (D)
DNA-bound (B)
$k_{ex,ED}$ = 51.8 s^{-1}
$k_{ex,DB}$ = 58.7 s^{-1}
p_D = 16.6 %
p_B = 2.7 %
B)
I/I0
35 Hz
29 Hz
25 Hz
16 Hz
9 Hz
15N (ppm)

Fig. S27.

Fits of CEST and DRD-CEST data of D34 to the D↔E↔B (A) and E↔D↔B (B) models. Black and red filled circles are CEST and DRD-CEST data respectively, acquired at the B_1 fields indicated in each plot. The data points are the same between corresponding sub-panels of panels A and B. Green and orange lines are the best global fits 5 B_1 field CEST and 3 B_1 field DRD-CEST data to the D↔E↔B model (A) and E↔D↔B model (B) for DNA binding. Cyan circles are simulated DRD-CEST data assuming the correct exchange mechanism is the E↔D↔B model. Simulations were done using the best-fit parameters obtained by fitting 5 CEST and 3 DRD-CEST globally to the E↔D↔B model ($k_{ex,DE}$ = 51.8 s^{-1}, $k_{ex,DB}$ = 58.7 s^{-1}, p_E = 16.6 % and p_B = 2.7 %). The sizeable difference between the experimental DRD-CEST data (orange) and the simulated data for the E↔D↔B model (cyan) confirms that the correct mechanism of exchange is the D↔E↔B model. Magenta boxes in panel B highlight systematic deviations between the CEST data and the fits for the E↔D↔B model that are not present in the corresponding fit to the D↔E↔B model. In panel B, the fits systematically underestimate the size of the minor dip at the chemical shift of the DNA-bound state in order to accommodate the expected DRD-CEST data, so that the fits to the DRD-CEST (orange lines) are also systematically deeper than the experimental data (red circles) and closer to the simulated datapoints (cyan).

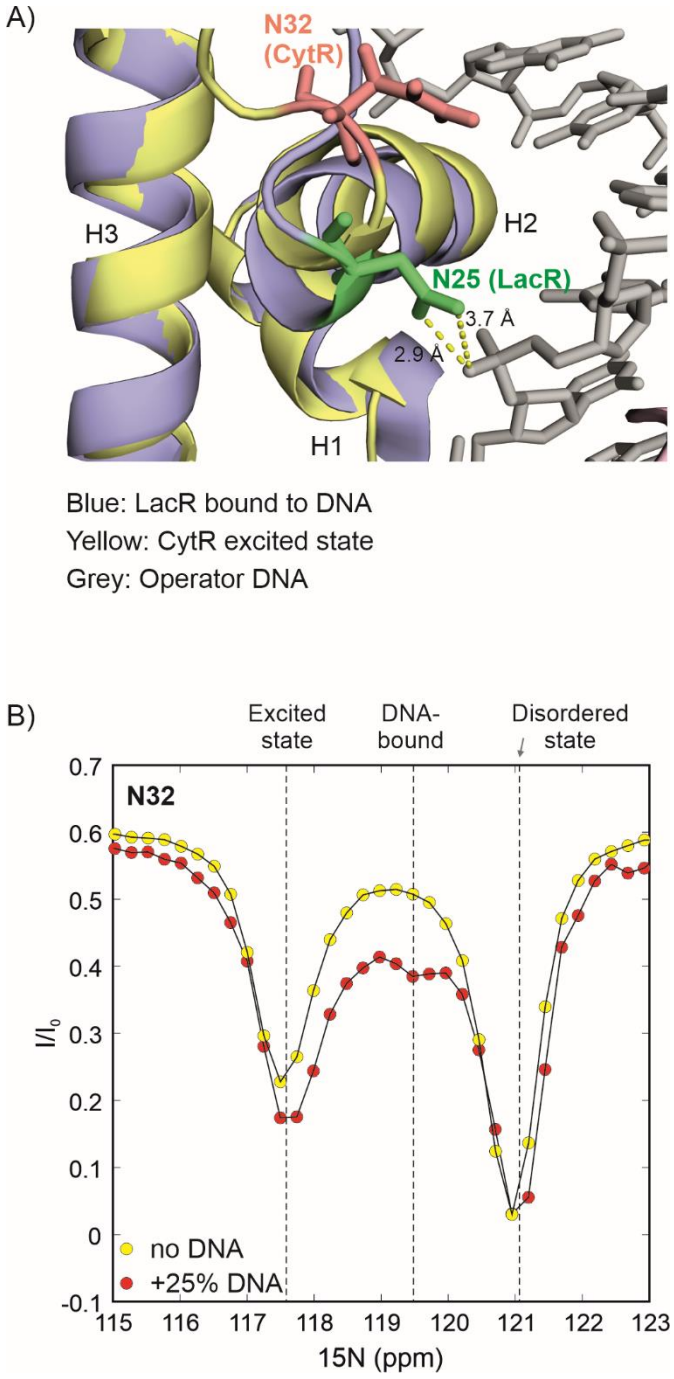

Fig. S28.

A) Overlay of DNA-bound LacR (blue, PDB ID 1EFA (*64*)) and the excited state of $CytR^N$ (yellow). The DNA molecule is shown as grey sticks. Helix H2 is slightly shorter in the excited state of $CytR^N$. The sidechain of N25 in LacR forms hydrogen bonds with the DNA phosphodiester backbone (*64*, *65*), while the corresponding residue in $CytR^N$ (N32) is further away and oriented differently, suggesting that this residue reorganizes itself after the folded state of $CytR^N$ binds DNA. In agreement with this, ^{15}N CEST profiles of N32 in a sample

containing DNA (B, red) show that N32 has a very different chemical shift in the DNA-bound form compared to the excited state.

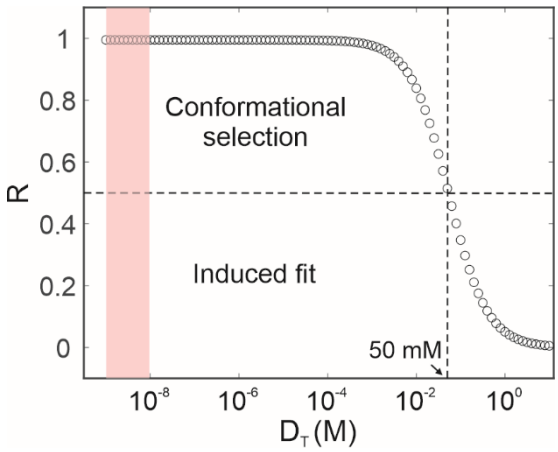

Fig. S29.

Plot depicting the total DNA concentration (D_T) dependence of the operative (CS vs IF) mechanism through the R value ($R = \frac{\phi_{CS}}{\phi_{CS}+\phi_{IF}}$) where ϕ_i is the flux along the i^{th} pathway ($i \in$ CS,IF). R=0 for the pure IF mechanism and R=1 for the pure CS mechanism. The pink shaded region corresponds to approximate DNA concentrations relevant inside an *E.coli* cell. The crossover between the CS and IF mechanisms (R=0.5) occurs at a D_T value of ~ 50 mM.

Table S1.
List of wt and mutant samples used for NMR experiments.

Sample number	Variant	Isotope labelling	Protein conc. (µM)	DNA conc. (µM)	Experiments carried out
1	Wt	^{13}C, ^{15}N	614	-	^{15}N CEST and backbone assignment experiments
2	Wt	^{15}N	648	-	^{15}N CEST, ^{15}N CPMG, temperature dependence
3	Wt	^{13}C, ^{15}N	713	-	$^{13}C\alpha$ CEST, $^{13}C\alpha$ Gly CEST, $^{1}H^{N}$ CEST, $^{13}C'$ CEST
4	Wt	^{15}N	690	-	^{15}N CEST, sample before DNA addition
5	Wt	^{15}N	628	150	^{15}N CEST, ^{15}N DRD-CEST
6	Wt	^{15}N	629	32	CPMG experiments on DNA-bound $CytR^{N}$
7	Wt	^{15}N	1060	-	Isotropic sample for PAG
8	Wt	^{15}N	980	-	Aligned sample (PAG)
9	Wt	^{15}N	793	-	Isotropic sample for C_8E_5/octanol
10	Wt	^{15}N	806	-	Aligned sample (C_8E_5/octanol)
11	A29V	^{15}N	1800	-	^{15}N CEST
12	V44A	^{15}N	1300	-	^{15}N CEST
13	A29V/A48M	^{13}C, ^{15}N	843	-	^{15}N CEST and backbone assignment experiments

Table S2.

p_E and $k_{ex,DE}$ obtained by fitting ^{15}N CEST or ^{15}N CPMG data acquired on various samples of free $CytR^N$.

Sample number	**p_E (%)**	**$k_{ex,DE}$ (s^{-1})**
1 (CEST)†	8.7 ± 0.1	45.9 ± 0.9
2 (CEST)	18.7 ± 0.4	50 ± 2
2 (CPMG)	21 ± 1	47 ± 2
4 (CEST)	15.9 ± 0.3	52 ± 1
Average*	14 ± 5	49 ± 3

***** Only numbers from CEST were used in calculating the average

† χ^2_{red} surfaces and errors in p_E and $k_{ex,DE}$ from Monte Carlo simulations for Sample 1 are shown in Figure S4 and are comparable to the errors from analysis of the covariance matrix evaluated during the fitting routine. Errors for all other samples are obtained from covariance matrix analysis.

Table S3.

p_E and $k_{ex,DE}$ obtained by fitting ^{15}N or multinuclear CEST profiles

S.No.	Nucleus	Number of residues	p_E (%)	$k_{ex,DE}$ (s^{-1})
1	^{15}N	12	8.7 ± 0.1	46 ± 1
2	^{15}N	39	8.2 ± 0.1	56 ± 1
3	^{15}N	39	9.0 ± 0.2	45 ± 1
	$^{13}C'$	32		
4	^{15}N	39	8.1 ± 0.1	59 ± 1
	$^{13}C'$	32		
	$^{1}H^{N}$	32		

^{15}N CEST data were acquired on Sample 1 while ^{13}C and $^{1}H^{N}$ data were acquired on Sample 3.

Table S4.

Parameters used for recording multinuclear CEST experiments on wt and mutant $CytR^N$.

Sample	Experiment	B_1 (Hz)	T_{ex} (ms)	sweep (Hz)	No. of planes	Offset spacing (Hz)	t_1 (ms)	t_2 (ms)
$CytR^N$ wt	^{15}N CEST	14.7	300	-720 to 720	98	15	64	40
	^{15}N CEST	28.6	300	-720 to 720	50	30	64	40
	$^{13}C'$ CEST	25	200	-900 to 900	62	30	64	38
	$^{1}H^N$ CEST	25	300	-1500 to 1500	102	30	64	33
	$^{13}C\alpha$ CEST	25	250	-1500 to 1500	102	30	64	31
	$^{13}C\alpha$ Gly CEST	25	250	-2220 to 1620	22	30	64	31
V44A $CytR^N$	^{15}N CEST	14.0	400	-720 to 723	113	13	64	42
	^{15}N CEST	26.5	400	-720 to 730	60	25	64	42
A29V $CytR^N$	^{15}N CEST	12.4	400	-720 to 723	113	13	64	42
	^{15}N CEST	23.9	400	-720 to 730	60	25	64	42

Table S5.

List of chemical shifts[1] of the wt $CytR^N$ excited state.

Res no.	ϖ_E (^{15}N)	ϖ_E ($^1H^N$)	ϖ_E ($^{13}C\alpha$)	ϖ_E ($^{13}C'$)
2	124.63		56.06	176.05
3	126.95	8.52	51.98	177.74
4	121.73	8.63		
5				176.30
6	123.34	8.56	55.76	175.96
7	123.52	8.64	56.58	176.79
8	116.48	8.38	61.38	
9	127.51	8.50	52.40	178.13
10	123.96	8.36	52.22	178.70
11	112.40	9.34		
12				176.79
13			58.78	
14	118.84	7.43	57.60	
15	119.40	7.38	65.75	176.67
16	122.89	8.36		
17	116.71	8.06	57.32	180.01
18	119.09	7.40	57.36	177.72
19	118.84	8.53		
20	115.38	8.06		
21			58.59	174.60
22	114.69	8.56		176.17
23	115.85	9.05	66.83	176.89
24	123.73	8.34	55.20	180.46
25	118.08	7.91	66.90	175.62
26	121.38	7.77	67.20	176.41
27	111.88	8.11		
29	118.00		54.73	178.54
30	112.33	7.87	56.35	179.03
31	116.18	8.30	56.38	176.75
32	117.54	8.48		
33			65.43	177.00
34	113.90	8.52	55.14	176.83
35	117.38	8.29		
37	117.83	8.86	57.97	175.08
38	123.01	9.09	59.43	177.88
39	120.06	8.61	55.45	181.22
40	117.92	7.96	66.87	175.57
41	122.50	8.67		

42	116.46	8.65		177.85
43			59.31	
44	120.31	8.32		
45				177.96
46	119.28	7.96		
47	120.71	7.45	54.87	178.92
48	118.74	8.85	55.20	179.99
49	118.41	8.02		
50				179.24
51	108.56	7.91	60.75	175.87
52	109.46	7.61	45.86	174.71
53	121.47	8.35	59.37	173.98
54	125.89	7.44		
55				176.71
56	119.48	8.74		
57				177.16
58	120.53	8.58	55.55	177.10
59	110.33	8.46	45.15	174.18
60	120.20	8.30	56.36	176.13
61	119.75	8.26	52.89	175.26
62	120.31		62.52	176.22
63	125.53	8.42	56.46	176.41
64	123.23	8.48	56.34	175.63
65	120.88	8.63	53.61	174.23
66	126.11	7.98		

[1] The average errors in the chemical shifts of the excited state extracted with ChemEx were of the order of 0.01 ppm in ^{15}N, 0.003 ppm in $^{1}H^{N}$, 0.03 ppm in $^{13}C\alpha$ and 0.09 ppm in ^{13}C'.

Table S6.

Parameters used for recording ^{15}N and $^{1}H^{N}$ CEST profiles in isotropic and aligned media.

Sample No.	Sample No.	Spectrometer (MHz)	Experiment	B_1 (Hz)	CEST sweep (Hz)	T_{ex} (ms)	No. of planes
7	Isotropic (for polyacrylamide)	Agilent 600 MHz	^{15}N CEST (coupled)	8	-750 to +750	400	127
			$^{1}H^{N}$ CEST	15	-1000 to +1000	500	102
8	Aligned (polyacrylamide stretched gel)	Agilent 600 MHz	^{15}N CEST (coupled)	8	-750 to 750	400	127
			$^{1}H^{N}$ CEST	15	-1000 to +1000	500	102
9	Isotropic (for C_8E_5/octanol)	Bruker 700 MHz	^{15}N CEST (coupled)	10	-876 to +876	400	148
			$^{1}H^{N}$ CEST	15	1370 to 3470	500	107
10	Aligned (C_8E_5/octanol)	Bruker 700 MHz	^{15}N CEST (coupled)	10	-876 to +876	400	148
			$^{1}H^{N}$ CEST	15	1370 to 3470	500	107

Table S7.

List of ^{15}N-^{1}H RDCs of the excited state of $CytR^{N}$ used in CS-Rosetta structure calculations.

Residue number	Polyacrylamide gel (PAG)	Residue number	C_8E_5/n-octanol
T11	1.1±1.9	T11	6.0±1.8
D14	0.7±3.1	D14	-0.7±3.4
V15	6.2±1.5	V15	9.0±2.9
A16	3.9±1.4	A16	7.0±1.9
L17	-1.5±0.8	L17	-4.9±1.8
K18	4.6±1.4	K18	1.0±1.8
A19	4.6±1.5	A19	3.0±2.8
K20	-9.8±2.4	K20	-15.9±4.3
V21	-7.7±1.5	S22	-20.4±3.6
S22	-14.1±0.6	T23	16.0±2.6
T23	3.6±1.4	A24	13.1±2.0
A24	3.8±3.4	T25	6.0±2.2
T25	-2.5±1.7	V26	8.0±3.5
V26	-0.5±1.4	S27	18.0±2.2
S27	4.4±1.8	A29	10.6±4.4
A29	-3.1±3.3	L30	12.0±2.9
L30	3.2±0.8	M31	14.4±2.3
M31	5.4±2.4	N32	9.7±2.6
N32	0.7±0.7	D34	7.7±2.4
D34	4.6±2.5	V36	7.0±1.9
K35	-12.7±1.3	S37	14.0±2.2
V36	5.5±1.7	Q38	-15.0±3.1
S37	2.6±1.3	A39	-29.0±2.8
Q38	-4.1±1.9	T40	-19.2±3.1
A39	-6.2±1.6	R41	-19.0±2.9
T40	-12.9±0.8	R43	-18.0±2.1
R41	-11.9±1.5	K46	-10.0±2.3
N42	-11.5±1.1	A47	-23.0±9.9
R43	-8.3±1.5	A48	-22.0±4.5
K46	-1.6±1.6	V51	-14.0±4.4
A47	-9.3±1.6	G52	-6.0±1.9
A48	-10.6±1.7	Y53	-2.0±2.4

V51	-10.5±2.1
G52	-4.0±1.2
Y53	0.3±1.2

Table S8.

Parameters used for recording CEST and DRD-CEST on Sample 5. CEST data were acquired using the D-CEST pulse sequence.

	Experiment	B_1 (Hz)	T_{ex} (ms)	sweep (Hz)	No. of planes	Offset spacing (Hz)	sw_{DANTE} (Hz)
1	^{15}N CEST	8.8	300	-350 to 350	72	10	700
2	^{15}N CEST	15.9	300	-272 to 272	36	16	544
3	^{15}N CEST	24.8	300	-450 to 450	38	25	900
4	^{15}N CEST	29.0	300	-465 to 465	33	30	930
5	^{15}N CEST	34.7	300	-450 to 450	32	30	900
6	^{15}N DRD- CEST	25.0	300	-350 to -100	12	25	254
7	^{15}N DRD- CEST	29.0	300	-350 to -100	12	25	254
8	^{15}N DRD- CEST	34.9	300	-350 to -100	12	25	254